Volume 8 Number 2 2020

STUDENT JOURNAL OF PHYSICS

INTERNATIONAL JOURNAL

INDIAN ASSOCIATION OF PHYSICS TEACHERS

ISSN – 2319-3166

STUDENT JOURNAL OF PHYSICS

This is a quarterly journal published by Indian Association Of Physics Teachers. It publishes research articles contributed by Under Graduate and Post Graduate students of colleges, universities and similar teaching institutions, as principal authors.

Registered Office

Editor-in-Chief, SJP, Institute of Physics, Sainik School, Bhubaneswar, Odisha, India – 751005
(www.iopb.res.in/~sjp/)

STUDENT JOURNAL OF PHYSICS

Scope of the Journal

The journal is devoted to research carried out by students at undergraduate level. It provides a platform for the young students to explore their creativity, originality, and independence in terms of research articles which may be written in collaboration with senior scientist(s), but with a very significant contribution from the student. The articles will be judged for suitability of publication in the following two broad categories:

1. **Project based articles**
   These articles are based on research projects assigned and guided by senior scientist(s) and carried out predominantly or entirely by the student.
2. **Articles based on original ideas of student**
   These articles are originated by the student and developed by him/ her with possible help from senior advisor. Very often an undergraduate student producing original idea is unable to find a venue for its expression where it can get due attention. SJP, with its primary goal of encouraging original research at the undergraduate level provides a platform for bringing out such research works.
   It is an online journal with no cost to the author.

Since SJP is concerned with undergraduate physics education, it will occasionally also publish articles on science education written by senior physicists.

Information for Authors

- Check the accuracy of your references.
- Include the complete source information for any references cited in the abstract. (Do not cite reference numbers in the abstract.)
- Number references in text consecutively, starting with [1].

- Language: Papers should have a clear presentation written in good English. Use a spell checker.

Submission

1. Use the link "Submit" of Website to submit all files (manuscript and figures) together in the submission (either as a single .tar file or as multiple files)
2. Choose one of the Editors in the link "Submit" of Website as communicating editor while submitting your manuscript.

Preparation for Submission

Use the template available at "Submit" section of Website for preparation of the manuscript.

Re-Submission

- For re-submission, please respond to the major points of the criticism raised by the referees.
- If your paper is accepted, please check the proofs carefully.

Scope

- SJP covers all areas of applied, fundamental, and interdisciplinary physics research.

STUDENT JOURNAL OF PHYSICS

Magnetic Skyrmions in Condensed Matter Physics*

Sayantika Bhowal, ** **S. Satpathy, and Pratik Sahu**
Department of Physics & Astronomy, University of Missouri, Columbia, MO 65211, USA
Date Received: 25/Dec/2019 Date Published: 21/Aug/2020

Abstract. Skyrmions were originally introduced in Particle Physics as a possible mechanism to explain the stability of particles. Lately the concept has been applied in Condensed Matter Physics to describe the newly discovered topologically protected magnetic configurations called the magnetic Skyrmions. This elementary review introduces the concept at a level suitable for beginning students of Physics.
Keywords: Skyrmions, Winding number, Spin texture

1. INTRODUCTION

The basic objects of Classical Mechanics are stable particles, characterized by a non-zero mass, which live for ever. In contrast, at a fundamental level, elementary particles such as electrons and protons are described using quantum field theory, where they are thought of as wave-like excitations of an underlying field. It is however a non-trivial task in field theory to make these wave-like excitations stable; they would generally dissipate similar to the disappearance of the waves in a pond once they have been created. In the year 1962, Skyrme [1] proposed the idea that the particles do not decay because they are topologically protected, in the sense that they have a topological number, which can not be changed by a continuous deformation of the underlying field. In topology, a donut is topologically equivalent to a cup, as they both contain one hole, and one can be continuously deformed to the other. A sphere contains no hole and is topologically different, and thus can not be deformed into a donut by continuous deformation. Sometime later, it was pointed out that topologically protected systems may be relevant in condensed matter physics [2, 3]. Recently, there has been a flurry of theoretical and experimental works [4] showing that topologically protected states can be stabilized in chiral magnets in the form of a swirling spin texture called a "magnetic Skyrmion." The present review aims at introducing the basic concepts of the magnetic Skyrmion to beginning students of Physics.

2. MAGNETIC INTERACTION IN SOLIDS

In magnetic solids, such as Iron, atoms acquire a magnetic moment due to the spin of the electron, or in some cases due to its orbital motion. Arranged on a periodic lattice structure in the solid, the atomic moments interact with one another, leading to well defined magnetic structures such

* Written by experts on a current topic on the frontier of Condensed Matter Physics useful for the young aspiring researchers.
** bhowals@missouri.edu

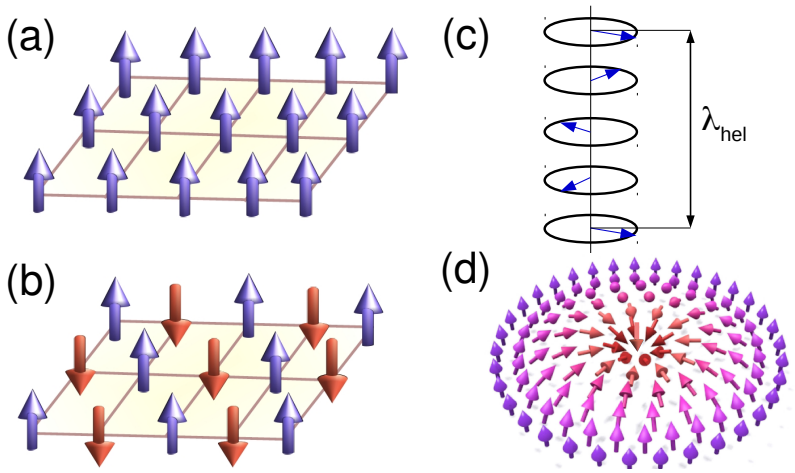

Figure 1. Different types of magnetic states in solid. (a) Ferromagnetic state, (b) Anti-ferromagnetic state (c) Helical state, and (d) Skyrmion state. For the ferromagnetic and the anti-ferromagnetic structures, magnetic moments of individual atoms are arranged as shown. In the helical state, ferromagnetic planes are stacked on top of one another, with their magnetic moments turning with the periodicity determined by the helical length $\lambda_{\rm hel}$. The Skyrmion state is characterized by a certain Skyrmion number as discussed in the text. (Fig. (d) is reproduced with permission from the authors of Ref. [5].)

as a ferromagnet or an anti-ferromagnet. The simplest Hamiltonian that describes the interaction between the magnetic moments is the Heisenberg Hamiltonian

$$\mathcal{H}_H = J \sum_{ij} \vec{S}_i \cdot \vec{S}_j, \tag{1}$$

where $\vec{S}_i$ is the (spin) magnetic moment at site i and J is the interaction between nearest neighbors. The sign of J determines the relative alignment of the spins, e.g., if $J < 0$, the spins prefer to align parallel to each other (ferromagnet) so that the energy is a minimum. On the other hand, a positive J leads to an antiparallel alignment resulting in an antiferromagnetic structure (See Fig. 1). In solids with strong spin-orbit coupling and broken inversion symmetry, a cross-product or chiral interaction, known as the Dzyaloshinskii-Moriya (DM) interaction exists. Although much smaller in magnitude than the Heisenberg interaction, the DM interaction can lead to fundamentally new Physics. The DM interaction reads

$$\mathcal{H}_{\rm DM} = \sum_{ij} \vec{D}_{ij} \cdot (\vec{S}_i \times \vec{S}_j), \tag{2}$$

where $\vec{D}$ is the strength of the DM interaction. In contrast to the Heisenberg interaction which only favors parallel or antiparallel alignment of the spins, the DM interaction favors a canted spin

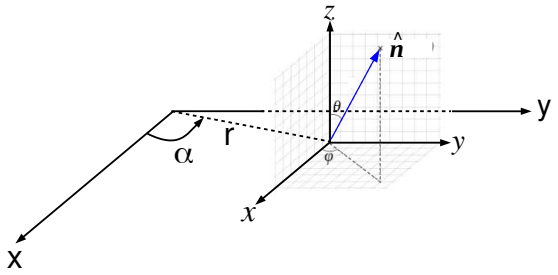

Figure 2. Polar coordinates to describe the spin texture in the continuum model of the Skyrmion state. The direction of the magnetization vector $\vec{n}(\vec{r})$ depends on its location $\vec{r}$ on the 2D plane, described by the polar coordinates (r, α), but $\vec{n}(r, \alpha)$ can point anywhere in 3D, described by the spherical coordinates θ and ϕ at each point $\vec{r}$. For the skrmion state, the polar angle $\theta(r)$ and the azimuthal angle $\phi(\alpha)$ are functions of only r and α, respectively. An electron moving in the spin texture $\vec{n}(\vec{r})$ experiences a topological electric amd magnetic field, caused by the fact that the electron spin must follow the local spin directions as it moves in the 2D space.

alignment (energy becomes minimum if the two spins are perpendicular to each other and lie on a plane normal to $\vec{D}$, as can be immediately seen from Eq. 2).

The presence of both the Heisenberg and the DM interactions leads to a helical spin state, and the DM interaction under certain conditions can lead to the Skyrmion state as well, which we will discuss shortly. In the simplest helical state, ferromagnetic planes of spins turn along the direction normal to the planes, with a helicity angle ϑ and the helical period $\lambda^{\rm hel} = 2\pi/\vartheta$ (Fig. 1 c). The helicity angle is determined by the minimization of the net energy, coming directly from the expressions for the Heisenberg and the DM interactions,

$$E(\vartheta) = JS^2 \cos\vartheta + DS^2 \sin\vartheta, \tag{3}$$

which leads to $\vartheta = \tan^{-1}(D/J)$. The helical period ($\lambda^{\rm hel}$) in some representative materials are listed in Table 1, which is indicative of the strength of the DM interaction.

3. THE SKYRMION STATE

The Skyrmion state is a complex magnetic state, the formation of which is mediated by one of several mechanisms [6–9], viz., (i) The DM interaction together with a magnetic field, (ii) Magnetic dipolar interaction, (iii) Frustrated exchange interaction, (iv) Four-spin interactions, and (v) Rashba spin-orbit coupling in the presence of itinerant electrons (polaronic Skyrmion).

In addition, the Skyrmion state is defined such that $\theta(r)$ changes from $\theta = \pi$ at the center

Table 1. Néel temperatures (T_N) and helical periods ($\lambda^{\rm hel}$) in some of the magnetic materials with broken inversion symmetry.

Materials	T_N (K)	$\lambda^{\rm hel}$ (nm)
MnSi (Bulk)	30	18
MnSi (Thin film)	45	8.5
MnGe (T = 20 K)	170	3
$Mn_{0.5}Fe_{0.5}Ge$	185	14.5

to $\theta = 0$ at the boundary of the Skyrmion ($r = \lambda$) or vice versa. Single-valuedness of the spin orientation demands that the azimuthal angle is of the form

$$\phi(\alpha) = m\alpha + \gamma, \qquad (\text{winding number } m \text{ and helicity parameter } \gamma \text{ defined}) \quad (4)$$

A magnetic Skyrmion is a swirling magnetic structure of spins as illustrated in Fig 1. It is usually a two-dimensional (2D) object, existing at interfaces between two materials or in magnetic thin films. The topological properties depend on the geometry of the structure. The two key characteristic geometrical quantities are the vorticity and the helicity of the structure, which are a characteristic of how the spin orientation $\vec{n}(\vec{r})$ changes over space. Note that for the lattice, the position $\vec{r}$ takes discrete values, while in continuum models it is a continuous variable. The spin orientation at each point $\vec{r} \equiv (r, \alpha)$ on the 2D plane is described in the spherical coordinates by specifying the polar and azimuthal angles, $\theta(\vec{r})$ and $\phi(\vec{r})$, respectively, as indicated in Fig. 2. For the Skyrmion state, $\theta(\vec{r})$ is a function of the radial distance r only and $\phi(\vec{r})$ is a function of the polar angle α only, so that in the cartesian coordinates, the local magnetization vector is

$$\vec{n}(\vec{r}) = (\sin\theta(r)\cos\phi(\alpha), \sin\theta(r)\sin\phi(\alpha), \cos\theta(r)). \quad (5)$$

where $\phi(\alpha)$ is given in Eqn.(4) with m is a non-zero integer called the winding number. Skyrmions and anti-Skyrmions are defined as those for which the winding number is positive or negative, respectively. The helicity parameter γ takes specific values for helical states. If $\gamma = \pm\pi/2$, then the helicity $h = \pm 1$ (the two signs indicate left or right handedness), while for $\gamma = 0$ or π, we have a radial spin structure. The Skyrmion spin texture for the winding number $m = 1$ and for different helicity parameters $\gamma = 0, \pi, \pm\pi/2$ are shown in Fig. 3 for illustration.

Physically speaking, a 2D magnetic Skyrmion can be thought of as a topological object which is formed by a stereographic projection from a spherical "hedgehog" of spins as shown in Fig. 3, where the down spin at the south-pole is mapped onto the center of the 2D disk, while the up spin at the north-pole is mapped onto the edge circle of the disk, far off from the centre. The Skyrmion number N_{sk} denotes the number of times $\vec{n}(\vec{r})$ wraps around the unit sphere. As shown in Section 5, the Skyrmion number simply equals the winding number m apart from a sign. Note that for trivial magnetic structures, e.g., ferro and antiferromagnetic order, $N_{sk} = 0$, while for the example shown in Fig. 3, the Skyrmion number is one.

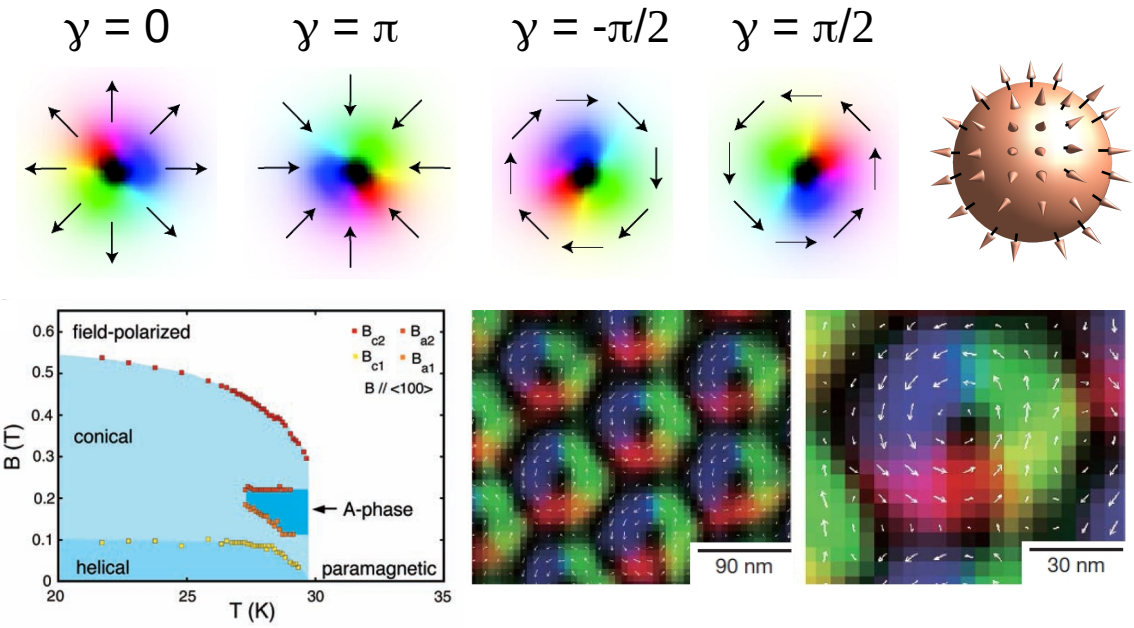

Figure 3. *Top panel:* Several Skyrmion spin structures corresponding to the winding number $m = 1$ and helicity parameter $\gamma = 0, \pi, \pm\pi/2$. The in-plane components of the spins are indicated by arrows, while the color map denotes the out of-plane component of the spin, where the black and white colors represent the down and up spin state, respectively. *Top panel right:* The spherical "hedgehog" of spins, the stereographic projection of which leads to the 2D magnetic Skyrmion as discussed in the text. The figure corresponds to the winding number $m = 1$. *Bottom left:* The phase diagram of MnSi in the parameter space of temperature (T) and magnetic field (B), showing the stabilization of the Skyrmion phase (the so called "A-phase") with small external magnetic field. *Bottom middle:* The real space configuration of the Skyrmion crystal in $Fe_{0.5}Co_{0.5}Si$ subjected to a weak magnetic field. *Bottom right:* The magnified view of this Skyrmion spin texture. The direction of the spin at each point is described by the color map: black color denotes $\uparrow$ or $\downarrow$ spin and the white arrows denote the in-plane component. Figure reproduced with permission from: top panel, Ref. [4] © 2013 Springer Nature; bottom left, Ref. [10] © 2009 AAAS; bottom middel and right, Ref. [11] © 2010 Springer Nature.

Experimental observation – Skyrmions were first observed in the year 2009 in MnSi using neutron scattering [10], when the well-known A-phase of MnSi was identified as the Skyrmion phase (Fig. 3). As shown in the figure, the Skyrmion lattice was stabilized at the boundary between the paramagnetic phase and a long-range helimagnetic phase, under the application of a small external magnetic field. The DM interaction induced by the symmetry-breaking distortions in the B20

phase [12] plays a crucial role in stabilizing the Skyrmion state in MnSi. Since then, other experiments have confirmed the existence of the Skyrmion state in a large number of chiral magnets, such as MnGe, $Fe_{1-x}Co_xSi$, etc [13]. More recently, experiments have shown the emergence of the Skyrmion state in oxide heterostructures [14, 15], when subjected to an external electric field. Such magnetic Skyrmion states are shown to be tunable by the external electric field, which controls the DM interaction at the interface [15].

In solids, the Skyrmions often form a periodic lattice (the Skyrmion crystal), rather than occurring as a single isolated Skyrmion. The Skyrmion crystal has a lattice structure, different from the atomic lattice of the host with a lattice spacing $\sim 50 - 100$ times larger than that of the underlying atomic lattice. The Skyrmion crystal phase can be detected by neutron scattering and usually small-angle neutron scattering (SANS) is employed for this purpose. An alternative technique is the resonant X-ray scattering. While these are momentum-space techniques, other methods such as the scanning probe microscopy are suitable for the direct real-space detection of the Skyrmion crystal or the isolated Skyrmions at the nanometre scale.

4. SKYRMION FORMATION: THE DZYALOSHINSKII-MORIYA MECHANISM

In this Section, we describe the formation of the Skyrmion state due to the DM interaction, which is a key mechanism. For the Skyrmion state to form, its energy must be lower than other competing magnetic states. For this to happen, certain types of magnetic interactions need to be present. According to the scaling argument of Derrick [16], formation of the Skyrmion state requires an odd power of the spatial gradient of $\vec{n}(\vec{r})$ (note that $\vec{n}$ is simply the direction of the spin $\vec{S}$) in the energy expression. In these models, the magnitude of $\vec{S}$ remains the same everywhere in space, but their orientation can change depending on the interaction.

The simplest model that can host the Skyrmion state has the DM interaction, which contains the gradient $\vec{\nabla}\vec{n}$ to the first power. Using familiar notations, the Hamiltonian reads

$$\mathcal{H} = J\sum_{ij}\vec{S}_i\cdot\vec{S}_j + \sum_{ij}\vec{D}_{ij}\cdot(\vec{S}_i\times\vec{S}_j) - A_s\sum_i(S_i^z)^2 - B\sum_i S_i^z, \tag{6}$$

where we have considered a spin model for a 2D system, where J is the FM Heisenberg exchange interaction, D is the DM interaction, A_s is the single-ion anisotropy, and B is an external magnetic field. It can be immediately seen by inspection of the Hamiltonian in the continuum limit, Eq. (7), that the DM interaction contains the only odd-power gradient term and therefore without it, a Skyrmion can not exist.

For the purpose of illustration, we take the DM interaction of the form[17] $\vec{D}_{ij} = D\,\hat{r}_{ij}\times\hat{z}$, which may arise from the Rashba SOC at a 2D interface [17], and write the Hamiltonian (6) in the continuum limit. The result is

$$E = \int d^2r\Big[\frac{J}{2}\sum_{\mu=x,y,z}(\vec{\nabla}n^\mu)^2 + D(n^z\partial_x n^x - n^x\partial_x n^z - n^y\partial_y n^z + n^z\partial_y n^y) - A_s(n^z)^2 - Bn^z\Big], \tag{7}$$

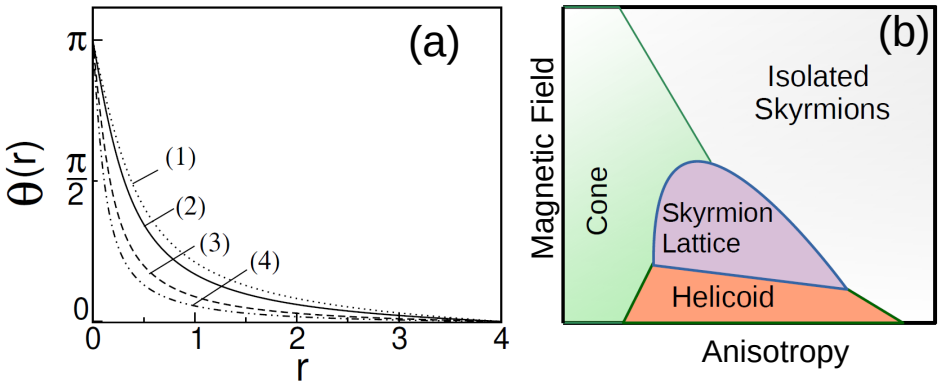

Figure 4. (a) Skyrmion solution of the second order differential equation (8) for the parameters (α, β, γ): (1) (0.2, 0.0, 0.1), (2) (0.2, 0.1, 0.0), (3) (0.2, 0.1, 0.1), and (4) (0.2, 0.1, 0.2). Here, the value of r, at which $\theta(r) = 0$, determines the Skyrmion size λ, which is a function of the parameters α, β, and γ, and has the typical value $\lambda \sim 100 - 1000$ Å in real materials. (b) The schematic phase diagram, adopted from Ref. [18], showing the equilibrium states for the model spin Hamiltonian (6) of a cubic helimagnet as a function of applied magnetic field (B) and uniaxial anisotropy (A_s). The scale of the magnetic field here is $B \sim 0.1 - 1$ Tesla, which is the typical value for which skyrmions have been observed in real materials (See Fig. 3).

where $\vec{\nabla} \equiv \hat{x}\partial_x + \hat{y}\partial_y$. Note that if $D = 0$, then a uniform ferromagnetic state ($\vec{n}$ along $\hat{z}$) has the lowest energy, since any spatial deviation of the spin direction from $\hat{z}$ increases the total energy, and therefore any other state including the Skyrmion state would have a higher energy. This is a simple consequence of Derrick's stability criterion, since if $D = 0$ in the energy expression (7), then no odd power of $\vec{\nabla}\vec{n}$ is present anymore. Substituting the spin texture for the Skyrmion, Eq. (5), in the energy expression (7) and after some straightforward algebra, we get the expression for the energy of the Skyrmion state

$$E = 2\pi \int r dr \Big[\frac{J}{2}(\dot{\theta}_r^2 + \sin^2\theta/r^2) + D(\dot{\theta}_r + \sin 2\theta/2r) - A_s \cos^2\theta - B\cos\theta\Big], \quad (8)$$

where we have considered a Skyrmion with unit vorticity ($m = 1$).

The problem now boils down to the minimization of the energy, which can be done using the standard methods of the calculus of variations, which leads to the Euler equation

$$\frac{d}{dr}\Big(\frac{\partial F}{\partial \dot{\theta}_r}\Big) = \frac{\partial F}{\partial \theta}, \quad (9)$$

where $F \equiv F(\theta, \dot{\theta}_r, r)$ is the integrand in (8). Taking the derivatives, we immediately get a second-order differential equation

$$\ddot{\theta}_r + \dot{\theta}_r/r + \alpha \sin^2\theta/r - \beta \sin 2\theta - \sin 2\theta/r^2 - \gamma \sin\theta = 0, \tag{10}$$

where we have defined the scaled parameters $\alpha = 2D/J$, $\beta = A_s/J$, and $\gamma = B/J$. These are the scaled DM, anisotropy, and the magnetic field parameters, respectively.

The solution of the differential equation is obtained with the finite difference method with the boundary conditions: $\theta(r = 0) = \pi$ and $\theta(r \to \infty) = 0$, with various values of the parameters α, β and γ. The results are shown in Fig. 4 (a), which indicate the formation of an isolated Skyrmion state. Note that the magnetic field (parameter γ) aids in the formation of the Skyrmion state, and as the strength of the field is increased, the size of the Skyrmion becomes smaller and smaller.

So far we have discussed the role of the DM interaction in the formation of an isolated Skyrmion state in 2D. In reality, other spin textures such as the cone phase and the helicoid structure can also be stabilized. The stabilizations of these different magnetic states as a function of external magnetic field and anisotropy are discussed in Ref. [18] in the context of cubic helimagnets. A schematic of this phase diagram is shown in Fig. 4 (b).

5. DYNAMICS OF ELECTRONS IN THE PRESENCE OF A SKYRMION: THE TOPOLOGICAL MAGNETIC FIELD

In this Section, we discuss the forces acting on an itinerant electron as it moves through the Skyrmion state, with the local space fixed magnetic moments defined by $\vec{n}(\vec{r})$. The topological electromagnetic fields are effective fields that the electron sees on account of its motion in the network of the localized moments. We assume a strong Hund's coupling, which means that the only possible spin state of the electron is the one parallel to the magnetization vector of the local spin. Thus as the electron moves about in space, its spin must conform to the local magnetization direction. An effective electromagnetic field arises, even though no external electric or magnetic field has been applied. These are the so called "emergent" or "topological" fields that the electron experiences because the local magnetization vector changes from point to point.

Let us consider an electron moving in a spatially varying spin texture of the Skyrmion state, with the local magnetization vector $\vec{n}(\vec{r})$ described by (θ, ϕ) in the spherical coordinates (see Fig. 2). We take the large Hund's coupling limit ($J_H \to \infty$, typically a few eV in the solid), so that the electron spin is everywhere parallel to the local moment as it moves about in the presence of the Skyrmion. Thus the spin wave function of the electron can be written as

$$|\chi(\vec{r})\rangle = \begin{bmatrix} \cos\frac{\theta(r)}{2} e^{-i\phi(\alpha)} \\ \sin\frac{\theta(r)}{2} \end{bmatrix} \tag{11}$$

in the global spin up ($\uparrow$) and down ($\downarrow$) basis set. As a result, the spin of the electron rotates spatially as if it experiences an effective magnetic field $\vec{B}(\vec{r})$ and precesses about this magnetic field. This

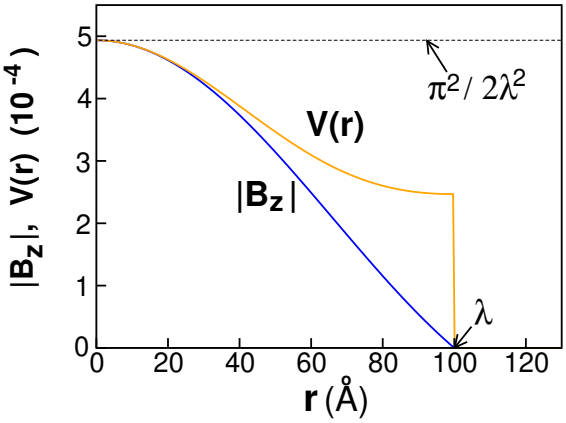

Figure 5. Spatial variations of the topological magnetic field (17) and the scalar potential $V(r)$ (18) for the Skyrmion profile, Eq. (16). The radius of the Skyrmion λ is taken to be 100 Å. For this figure, we have taken $\hbar = c = e = 1$.

physical picture is easy to follow from the kinetic energy of the conduction electron moving in a Skyrmion spin texture $\vec{n}(\vec{r})$,

$$E_{kin} = \langle\Psi|(-\hbar^2\nabla^2/2m)|\Psi\rangle, \tag{12}$$

where the wave function is a direct product of a spatial part and a spin part, viz.,

$$|\Psi\rangle = \psi(\vec{r})\chi(\vec{r}\sigma). \tag{13}$$

Writing $\nabla^2 = \partial_r^2 + \frac{1}{r}\partial_r + \frac{1}{r^2}\partial_\alpha^2$ and $|\Psi\rangle = \psi(r,\alpha)(\cos\frac{\theta(r)}{2}e^{-i\phi(\alpha)}|\uparrow\rangle + \sin\frac{\theta(r)}{2}|\downarrow\rangle)$, and taking into account the symmetry of the Skyrmion i. e., $\theta \equiv \theta(r)$ and $\phi \equiv \phi(\alpha)$, after some algebra we get the kinetic energy of the electron

$$\begin{aligned} E_{kin} &= \frac{-\hbar^2}{2m}\int d^2r\Big[\psi^\star\nabla^2\psi - |\psi|^2\Big(\frac{\dot{\theta}_r^2}{2} + \frac{\dot{\phi}_\alpha^2\cos^2\theta/2}{r^2}\Big) - i\frac{2\dot{\phi}_\alpha\cos^2\theta/2}{r^2}\psi^\star\dot{\psi}_\alpha\Big] \\ &= \frac{1}{2m}\int d^2r\ \psi^\star\Big[(\vec{p} - e\vec{A}/c)^2 + V\Big]\psi, \end{aligned} \tag{14}$$

where $\vec{p} \equiv -i\hbar\vec{\nabla}$, $e < 0$ is the charge of the electron, and the derivatives are indicated by the subscripts, e.g., $\dot{\psi}_\alpha \equiv \partial\psi/\partial\alpha$. Also, here, $V = 4^{-1}\hbar^2\Big(r^{-2}\dot{\phi}_\alpha^2\sin^2\theta + \dot{\theta}_r^2\Big)$, $\vec{A} = \frac{\Phi_0}{2\pi r}(\dot{\phi}_\alpha\cos^2\theta/2)(\hat{r}\times\hat{z})$ with V and $\vec{A}$ being the scalar and the vector potentials respectively, and $\Phi_0 = hc/e$ is the flux quantum in cgs units. The scalar potential corresponds to a radially outwards force, while the vector

potential $\vec{A}$ leads to the topological magnetic field

$$\begin{aligned}\vec{B}(\vec{r}) &= \vec{\nabla} \times \vec{A} = \hat{z}(\partial_x A_y - \partial_y A_x) = \hat{z}\frac{\Phi_0}{2\pi}\frac{\dot{\theta}_r \dot{\phi}_\alpha \sin\theta}{2r} \\ &= \frac{\Phi_0}{4\pi}\vec{n}\cdot\Big(\partial_x\vec{n}\times\partial_y\vec{n}\Big)\hat{z}. \quad \text{(topological magnetic field)}\end{aligned} \tag{15}$$

We pause here to consider the special case where the magnetization vector $\vec{n}$ points along $\hat{z}$ everywhere ($\theta = \phi = 0$), for example, for the case of the ferromagnetic state. Then clearly both the scalar and vector potentials are zero from the above expressions and the electron moves as a free particle. In the Skyrmion state, however, the electron experiences a spatially varying topological magnetic field. Let us assume the Skyrmion profile

$$\begin{aligned}\theta(r) &= \pi(1 - r/\lambda),\ r \le \lambda \\ &= 0,\ r > \lambda \\ \text{and} \quad \phi(\alpha) &= \alpha,\end{aligned} \tag{16}$$

where λ denotes the Skyrmion radius. Using these functional forms of $\theta(r)$ and $\phi(\alpha)$, it is easily seen that the topological magnetic field is along $\hat{z}$ with the magnitude

$$\begin{aligned}B_z &= -\frac{\Phi_0}{4\lambda r}\sin(\pi r/\lambda),\ \text{if}\ \ r \le \lambda \\ &= 0\ ,\ \text{if}\ \ r > \lambda,\end{aligned} \tag{17}$$

and

$$\begin{aligned}V(r) &= 4^{-1}\hbar^2\Big[\frac{\sin^2(\pi r/\lambda)}{r^2} + \frac{\pi^2}{\lambda^2}\Big],\ \text{if}\ \ r \le \lambda \\ &= 0\ ,\ \text{if}\ \ r > \lambda.\end{aligned} \tag{18}$$

The spatial variation of these quantities are shown in Fig. 5. As can be seen from these plots, at the centre of the Skyrmion ($r \to 0$) $|B_z| = V(r) = \pi^2/2\lambda^2$. For typical Skyrmion radius $\lambda = 100$ Å, this leads to a large topological magnetic field ($\sim 10^2$ Tesla), which thus provides a unique platform to study the high magnetic field response of electrons [19].

Tight-Binding description – In the above analysis, we obtained the topological magnetic field from a continuum description, while in the solids, the Skyrmions exist of course on crystal lattices. A different way of obtaining the topological magnetic field is to consider the phase accumulated by the traveling electron in the lattice. As the electron travels, its spin must follow the fixed local magnetization direction $\vec{n}(\vec{r})$ adiabatically, as we already discussed. The hopping matrix element between two lattice sites a and b, in the tight-binding theory becomes

$$t_{ab} = \langle\Psi_a|H|\Psi_b\rangle = \langle\psi_a|H|\psi_b\rangle \times \langle\chi_a|\chi_b\rangle = te^{i\eta}, \tag{19}$$

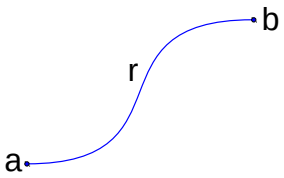

Figure 6. In the presence of a magnetic field, the amplitude to go from point a to point b acquires an extra phase factor $\left[\exp\left(\frac{ie}{\hbar c}\int_a^b \vec{A}\cdot\vec{dr}\right)\right]$, where $\vec{A}$ is the magnetic vector potential, as discussed in the Feynman Lecture Notes [20]. This modifies the hopping amplitude in the tight-binding theory as indicated in Eq. 20.

where $t = \langle\psi_a|H|\psi_b\rangle$ is the electron hopping without the spin texture and in the last equality, we have assumed a slowly varying spin texture (i. e., change in θ and ϕ between nearest neighbors in the lattice is assumed to be small). As is well known from the seminal book by Feynman [20], when an electron moves in a magnetic field, it acquires a phase factor (see Fig. 6), viz.,

$$t_{A\neq 0} = t_{A=0} \times \exp\left(\frac{ie}{\hbar c}\int_a^b \vec{A}\cdot\vec{dr}\right). \tag{20}$$

Comparing Eqs. (19) and (20), it is clear that even though no external magnetic field is present, the adiabatic motion of the electron in the spin texture is equivalent to a magnetic field, the "topological" magnetic field. Expressing the phase factor in Eq. (19) in terms of the Skyrmion texture $\theta(\vec{r})$ and $\phi(\vec{r})$ and after some straightforward algebra, one again gets the expression Eq. (15) for the topological magnetic field $\vec{B}(\vec{r})$.

Magnetic flux through the Skyrmion – It is easy to show that the flux through the Skyrmion due to the topological magnetic field is an integer multiple (the Skyrmion number N_{sk}) of the flux quantum Φ_0. Computing the flux through the 2D surface containing the Skyrmion with the magnetic field Eq. (15), we have

$$\Phi = \int_S \vec{B}\cdot d\vec{S} = \frac{\Phi_0}{4\pi}\int \left[\vec{n}\cdot\left(\partial_x\vec{n}\times\partial_y\vec{n}\right)\right] dS = \Phi_0 N_{sk}, \tag{21}$$

where the Skyrmion number N_{sk} characterizes the swirling structure of the Skyrmion. The fact that the Skyrmion number is an integer is a simple consequence of the boundary conditions imposed on $\vec{n}(\vec{r})$ to define the Skyrmion state. Using the Skyrmion spin texture Eq. (5), we can immediately see that the Skyrmion number is simply the winding number m times a sign $\eta = \pm 1$,

$$N_{sk} = \frac{1}{4\pi}\int_0^\infty dr\sin\theta(r)\dot{\theta}_r \times \int_0^{2\pi} d\alpha\,\dot{\phi}_\alpha = \eta m. \tag{22}$$

The quantity $\eta = \frac{1}{2}\cos\theta(r)|_{r=0}^{r=\infty} = \pm 1$ is related to the magnetization direction at the origin, i. e., if the spins point up at the origin $(r = 0)$ and down at $r \to \infty$, then $\eta = +1$, and it is -1 in the opposite case.

6. SKYRMIONIC POLARON

In this Section, we discuss the idea whether an electron can nucleate a Skyrmion state. The term "Skyrmionic polaron" has been recently coined [9] to describe such a system, which is analogous to the standard polaron state, which is a combination of an electron and the distorted lattice, which together form a localized state due to the electron-phonon interaction.

Interfaces are of interest because they are fertile grounds for the experimental observation of the Skyrmions. It has been recently suggested that the Skyrmionic polaron may exist at the interface between two solids, aided by the so called Rashba spin-orbit coupling [21]. The idea is that due to the broken mirror symmetry, an electric field perpendicular to the interface plane can exist, and if a large spin-orbit coupling is present, they both together lead to the momentum-dependent spin splitting of the electron states at a surface or interface, known as Rashba effect [21].

Rashba spin-orbit interaction – The Rashba interaction is a relativistic effect, originating from the coupling between the spin and the orbital degrees of freedom, when an electric field is present along a certain direction. This happens in solids when the mirror symmetry is broken, e.g., at the surface or at the interface between two materials. The Rashba interaction is described by the Hamiltonian

$$\mathcal{H}_R = \alpha_R(\sigma_x k_y - \sigma_y k_x), \tag{23}$$

where $\vec{k}$ is the electron momentum, $\vec{\sigma} = (\sigma_x, \sigma_y, \sigma_z)$ are the Pauli matrices, and α_R is the strength of the Rashba interaction. Diagonalization of (23) leads to the additional linear splitting term on top of the quadratic band structure energy, with the result $\varepsilon_k = (\hbar^2 k^2/2m) \pm \alpha_R k$.

The microscopic origin of the Rashba interaction is similar to the relativistic effect that leads to the well-known $\lambda \vec{L} \cdot \vec{S}$ term in the atoms. Consider an electron moving in an electric field $E\hat{z}$, relevant for the Rashba problem. Due to the relativistic effect, in its rest frame, the electron sees the electric field as a magnetic field $\vec{B} = -(\vec{v} \times \vec{E})/c^2$, which couples with the spin magnetic moment. The interaction energy is given by $\mathcal{H}_R = -\vec{M} \cdot \vec{B} = (g\mu_B \vec{\sigma}/2) \cdot (\vec{v} \times \vec{E})/c^2$. Writing $\vec{v} = \hbar\vec{k}/m$ and rearranging the terms, one immediately finds the Rashba Hamiltonian (23), with the Rashba coefficient α_R is expressed in terms of the various fundamental quantities. In addition, one can easily show that if instead of the uniform field along a fixed direction, the nuclear electric field along the radial direction is used, we would obtain the well-known $\lambda \vec{L} \cdot \vec{S}$ term in atomic physics.

The Rashba interaction leads to many interesting phenomena in condensed matter physics, but relevant for the present case is the fact that it produces a Dzyaloshiski-Moriya interaction $\vec{D} \cdot (\vec{S}_i \times \vec{S}_j)$ between two local spins [17], which facilitates the formation of a Skyrmion state by supporting a non-collinear alignment of the spins. So, the question that naturally arises is whether a single electron with the Rashba interaction in a 2D system can nucleate a Skyrmion state for the local spins.

Formation of the Skyrmionic polaron– Consider the following continuum model for a single electron moving in the Skyrmionic spin texture $\vec{n}(\vec{r})$ in the presence of the Rashba interaction. The

Hamiltonian is

$$\mathcal{H} = \frac{\hbar^2 k^2}{2m} - J\vec{n}\cdot\vec{\sigma} + (\sigma_x k_y - \sigma_y k_x) - b_z \int n_z(\vec{r})\, d^2r, \tag{24}$$

where we have added a magnetic field b_z normal to the plane for generality because in certain situations, the Skyrmion state is stabilized by a magnetic field, and the exchange coupling J between the local spin texture and the electron spin will be taken as ∞. The large $J \to \infty$ condition effectively renders this to a spinless problem as the electron spin is always parallel to the spin texture $\vec{n}(\vec{r})$ everywhere as the electron moves around. Switching to the spin basis to be along the local moments (Eq. 11), and modeling the Skyrmion texture $\vec{n}(\vec{r})$ again by the form: $\theta(r) = \pi(1 - r/\lambda),\ r \leq \lambda$, and 0 otherwise, and $\phi(\alpha) = \alpha$, the spinless electron experiences the magnetic field as well as a static potential given by Eqs. (17) and (18), respectively.

We can then proceed to obtain the ground state configuration of the Skyrmion by minimizing the total energy of the Hamiltonian (24) from the variational method, treating the Skyrmion radius λ as the single variational parameter. The average topological magnetic field has the value $\bar{B} = \Phi_0/(\pi\lambda^2)$ and the corresponding magnetic length $l = \lambda/\sqrt{2}$. The quantized electron states of the electron moving in a magnetic field are the Landau levels, with the lowest energy being $\hbar\omega_c/2 = \hbar^2/(m\lambda^2)$, ω_c being the cyclotron radius. The potential energy may be approximated as $\langle V(r)\rangle = V(l)$, where we simply evaluate the expression (18) for $V(r)$ at $r = l$.

The third term in the Hamiltonian (24) is the Rashba term. We evaluate the Rashba energy for the symmetric wave function $\psi(r)$, where there is no angular dependence α, with the result

$$H_R = \langle\psi(r)\uparrow|\alpha_R(k_x\sigma_y - k_y\sigma_x)|\psi(r)\uparrow\rangle = \frac{\alpha_R}{2}\int |\psi|^2 \times (\dot{\theta}_r - \frac{\dot{\phi}_\alpha}{r}\sin\theta)\, d^2r, \tag{25}$$

where $\uparrow$ denotes the spin aligned along the local moment and $\vec{k} \equiv -i\vec{\nabla}$. Evaluating this integral and putting together all energy terms, we finally arrive at the result

$$E(\lambda) = \frac{\hbar^2 a}{2m\lambda^2} + \pi b_z \lambda^2(1 - \frac{4}{\pi^2}) - \frac{\alpha_R b}{\lambda}, \tag{26}$$

where $a = \pi^2/4 + 2 + 2^{-1}\sin^2(\pi/\sqrt{2})$ and $b = \pi/2 + 2^{-1/2}\sin(\pi/\sqrt{2})$ are numerical constants, and the three terms are respectively the kinetic energy, the external magnetic field energy, and the Rashba energy. Minimizing the energy $dE(\lambda)/d\lambda = 0$ with no external magnetic field ($b_z = 0$), we obtain the Skyrmion radius and the corresponding ground state energy. The result is

$$\lambda_0 \approx \frac{2\hbar^2}{m\alpha_R}, \quad \text{and} \ \ E_0 \approx -\frac{3m\alpha_R^2}{4\hbar^2}. \tag{27}$$

Clearly, without any Rashba interaction ($\alpha_R = 0$), the Skyrmion radius λ_0 is infinity, indicating that there is no Skyrmion state, while the presence of the Rashba term favors the formation of the Skyrmion state with the binding energy E_0. The result is that the electron nucleates the Skyrmion state and in turn becomes bound inside it, forming thereby the "Skyrmionic polaron." From Eq. (26), it can be seen that an external magnetic field further aids in the formation of the Skyrmionic polaron, making its radius smaller and the binding energy larger.

7. APPLICATIONS AND FUTURE PERSPECTIVE

The topic of the magnetic Skyrmions has been rapidly developing over the past few years, both from the viewpoint of fundamental physics as well as the prospect for technological applications [22]. The Skyrmion spin texture is topologically stable with small thermal and quantum fluctuations, which makes it suitable for applications in memory devices. The unusual electron dynamics and transport properties such as the Topological Hall effect (THE) [4, 13, 23] could have important application in spintronics devices. While the first discovery of the Skyrmions occurred in bulk materials with chiral magnetic interactions, the realization that they can also be stabilized at the interfaces of magnetic multilayers [24] has opened up additional potential opportunities, including novel pathways for Skyrmion generation and manipulation.

A promising application involves the so called Topological Hall effect (THE). In the well-known classical Hall effect, discovered by Edwin H. Hall in 1879, when a current carrying conductor is placed in a magnetic field, the charges experience a Lorentz force in a direction perpendicular to both the magnetic field and the current flow. In contrast to this, in the Topological Hall effect, it is the topological magnetic field of a non-collinear spin system such as the Skyrmion gives rise to the Lorentz force on the conduction electron, resulting in a different type of Hall effect. At the same time, the motion of the Skyrmion itself leads to a temporal variation of the topological magnetic field. This, in turn, induces an electromotive force or potential according to the Faraday's law. This topological electric field gives an additional contribution to the Hall effect. This has been observed recently in epitaxial thin films and even in nanowires, demonstrating the physical reality of the topological electromagnetic fields in solids [25].

A large number of Skyrmion based innovative devices have been recently proposed [26–28], although there remains several important issues to be resolved [22] before practical applications can be made. A notable Skyrmion based memory device is the Skyrmion racetrack memory, which has received considerable attention [26]. While a prototype racetrack memory has been successfully demonstrated, a practical electrical read-out scheme still remains to be developed. Another intriguing idea is the use of a single Skyrmion as the information bit [29]. Research on the magnetic Skyrmions is currently in its infancy, with rapid development in the fundamental physics and applications expected in the coming years.

8. ACKNOWLEDGMENTS

We thank the U.S. Department of Energy, Office of Basic Energy Sciences, Division of Materials Sciences and Engineering for financial support under Grant No. DEFG02-00ER45818.

References

[1] Skyrme, T. H. R. 1962, "A unified field theory of mesons and baryons", Nucl. Phys. **31**, 556-569

[2] Bogdanov, A. N. and Yablonskii, D. A. 1989, "Thermodynamically stable vortices in magnetically ordered crystals: The mixed state of magnets", Soviet Phys. JETP **68**, 101-103

[3] For a review, see: Salomaa, M. and Volovik, G. E. 1987, "Quantized vortices in superfluid ^{3}He", Rev. Mod. Phys. **59**, 533-613

[4] For a review of recent works, see: Nagaosa, N. and Tokura, Y. 2013, "Topological properties and dynamics of magnetic Skyrmions", Nature Nanotechnol. **8**, 899-911

[5] Mechelen, T. V. and Jacob, Z. 2019, "Viscous Maxwell-Chern-Simons theory for topological electromagnetic phases of matter", arXiv:1910.14288v1 (2019); Mechelen, T. V. and Jacob, Z. 2019, "Nonlocal topological electromagnetic phases of matter", Phys. Rev. B **99**, 205146.

[6] Garel, T. and Doniach, S. 1982, "Phase transitions with spontaneous modulation - the dipolar Ising ferromagnet," Phys. Rev. B **26**, 325-329

[7] Heinze, S. *et al.* 2011, "Spontaneous atomic-scale magnetic Skyrmion lattice in two dimensions," Nature Phys. **7**, 713-718

[8] Okubo, T., Chung, S. and Kawamura, H. 2012, "Multiple-q states and the Skyrmion lattice of the triangular-lattice heisenberg antiferromagnet under magnetic fields," Phys. Rev. Lett. **108**, 017206

[9] Brey, L. 2017," Magnetic Skyrmionic Polarons," Nano Lett. **17**, 7358-7363

[10] Mühlbauer, S., Binz, B. , Jonietz, F. , Pfleiderer, C. , Rosch, A., Neubauer, A., Georgii, R. and Boni, P. 2009, " Skyrmion lattice in a chiral magnet," Science **323**, 915

[11] Yu, X. Z. , Onose, Y., Kanazawa, N., Park, J. H., Han, J. H., Matsui, Y., Nagaosa, N. and Tokura, Y. 2010, "Real-space observation of a two-dimensional skyrmion crystal", Nature **465**, 901-904

[12] Shanavas, K. V. and Satpathy, S. 2016, "Electronic structure and the origin of the Dzyaloshinskii-Moriya interaction in MnSi," Phys. Rev. B **93**, 195101

[13] Yu, X. Z. , Kanazawa, N., Onose, Y., Kimoto, K., Zhang, W. Z., Ishiwata, S., Matsui, Y. and Tokura, Y. 2011, "Near room-temperature formation of a Skyrmion crystal in thin-films of the helimagnet FeGe," Nat. Mater. **10**, 106

[14] Ohuchi, Y. *et al.* 2018, "Electric-field control of anomalous and topological Hall effects in oxide bilayer thin films," Nat. Commun. **9**, 213

[15] Wang, L. *et al.* 2018, "Ferroelectrically tunable magnetic Skyrmions in ultrathin oxide heterostructures", Nat. Mater. **17**, 1087-1094

[16] Derrick, G. H. 1964, "Comments on Nonlinear Wave Equations as Models for Elementary Particles", J.Math. Phys., **5**, 1252

[17] Mohammad, M. V. and Satpathy, S. 2018, "Dzyaloshinskii-Moriya interaction in the presence of Rashba and Dresselhaus spin-orbit coupling", Phys. Rev. B, **97**, 094419

[18] Wilson, M. N. , Butenko, A. B., Bogdanov, A. N. and Monchesky, T. L. 2014, "Chiral Skyrmions in cubic helimagnet films: The role of uniaxial anisotropy", Phys. Rev. B, **89**, 094411

[19] Bruno, P., Dugaev, V. K. and Taillefumier, M. 2004, "Topological Hall effect and Berry phase in magnetic nanostructures", Phys. Rev. Lett., **93**, 096806

[20] The Feynman Lectures on Physics Vol III Ch. 21, "The Schrödinger Equation in a Classical Context: A Seminar on Superconductivity".

[21] Rashba, E. I. 1960, " Properties of semiconductors with an extremum loop. 1. Cyclotron and combinational resonance in a magnetic field perpendicular to the plane of the loop", Sov. Phys. Solid State **2**, 1109 ; Bychkov, Y. A. and Rashba, E. I. 1984, " Oscillatory effects and the magnetic susceptibility of carriers

in inversion layers", J. Phys. C **17**, 6039

[22] Finocchio, G., Büttner, F. , Tomasello, R., Carpentieri, M., Kläui, M. 2016 " Magnetic Skyrmions: from fundamental to applications", J Phys D Appl Phys, **49**, 423001

[23] Neubauer, A. *et al.* 2009, "Topological Hall effect in the A phase of MnSi", Phys. Rev. Lett. **102**, 186602

[24] Ranieri, E. D. 2014, "Skyrmions at the interface", Nature Nanotechnology **101**, 10.1038

[25] Schulz, T. *et al.* 2012, "topological electrodynamics of Skyrmions in a chiral magnet", Nature Phys. **8**, 301304

[26] Kang, W., Zheng, C., Huang, Y., Zhang, X., Zhou, Y., Lv, W., Zhao, W. 2016 "Complementary Skyrmion Racetrack Memory with Voltage Manipulation", IEEE Electron Device Letters, **37**, 924-927

[27] Liu, R.H., Lim, W.L. , Urazhdin, S. 2015 "Dynamical Skyrmion State in a Spin Current Nano-Oscillator with Perpendicular Magnetic Anisotropy", Phys. Rev. Lett. **114** , 137201

[28] Zhang, X. , Zhou, Y., Ezawa, M. , Zhao, G.P., Zhao, W. 2015 "Magnetic Skyrmion transistor: Skyrmion motion in a voltage-gated nanotrack", Sc. Rep. **5**, 11369
fundamental to applications", J Phys D Appl Phys, **49**, 423001

[29] Hagemeister, J., Romming, N., von Bergmann, K. , Vedmedenko, E.Y., Wiesendanger, R., 2015 " Stability of single Skyrmionic bits", Nat. Commun., **6**, 8455

STUDENT JOURNAL OF PHYSICS

Pion Decay Constant from Lattice QCD

Quintin E. Muhlenkamp [1**]

[1] Junior, Department of Physics, Wittenberg University, Springfield, Ohio, USA, 45504

Date Received: 31/Oct/2019 **Date Published: 21/Aug/2020**

Abstract. We present results for the value of the pion decay constant f_π, needed for understanding weak pion decay. We analyze lattice-QCD data from six ensembles generated by the MILC collaboration. Lattice spacings of $a \approx 0.06$, 0.09, and 0.12 fm are used, along with pion masses of $m_\pi \approx 130$, 220, and 310 MeV. Statistical errors are quantified and accounted for using jackknife resampling. Using a ground-state fit, the mass and decay constant are estimated for each ensemble. These estimates are then used to extrapolate the decay constant to the physical point. This procedure yields $f_\pi = 103.5(4.5)$ MeV with no QED correction and $102.7(4.7)$ MeV in the chiral limit.

Keywords: Pion Decay Constant, Lattice QCD

1. INTRODUCTION

The pion decay constant f_π is a multiplicative term used to describe the coupling of the charged pion to the mediating W boson in weak decay. The constant's precise value is important for checking a unitarity constraint on the Cabibbo-Kobayashi-Maskawa (CKM) matrix, which describes the inter-generational mixing of quark flavor. If f_π is known with small enough uncertainty, along with the kaon decay constant f_K, the matrix element V_{us} can be precisely determined, giving us insight into the possibility of new physics beyond the Standard Model. To improve the precision of the matrix element, we need theoretical work to decrease the uncertainty associated with its calculation. The goal of this work is, therefore, to use state-of-the-art lattice-QCD calculations to determine f_π and compare with other theoretical values.

Lattice QCD is a nonperturbative numerical technique used to investigate the properties of hadrons. Lattice must be used because of the complexity of the QCD vacuum associated with the Goldstone pion. Rather than an empty vacuum we would expect classically, the QCD vacuum introduces topological charge and the effects of chiral symmetry breaking that restrict the use of perturbative methods. Lattice QCD discretizes four-dimensional Euclidean space, then solves path integrals over configurations that are placed onto the lattice. During the discretization, a lattice of spacing a is laid over the hypercube, where vertices hold the quarks, and the connections hold the gluons. Data is then extracted with a correlation function, designed to work specifically with

** muhlenkampq@gmail.com

the set of lattice data. A correlation function contains operators at two points in spacetime and describes the evolution of a state from its source to sink [1]. The lattice gauge configurations of $N_f = 2 + 1 + 1$ were computed by the MILC collaboration [2]. The correlation functions were constructed by the PNDME collaboration [3]. To improve the distinction between the ground and excited states, the lattice operators are smeared. Smearing is equivalent to describing a hadron with a state created by an operator of nonzero spatial extent, rather than by a point. An example could be stretching the point into the shape of a gaussian distribution. This procedure helps improve the overlap of the creation and annihilation operators with the hadronic state of interest. Lattice QCD introduces deviations from the physical world such as discrete space and non-physical pion masses (used for computational convenience). However, these values can be extrapolated to physical ones as explained in the methodology.

2. METHODOLOGY

This work looks at two different types of smeared data. The first has both the source and sink smeared and is referred to as smear-smear; its correlation function looks like:

$$C_s(t) \approx \frac{Z_s^2}{2am_\pi} e^{-am_\pi t} = A_s e^{-am_\pi t} \tag{1}$$

where $C_s(t)$ is the correlator for the smear-smear dataset, Z_s is a measurement of the amount of overlap between the smeared operator and the pion ground state, t represents the number of time-steps between the source and sink, and am_π is the mass of the pion in lattice units. It should be noted that $\frac{Z_s^2}{2am_\pi}$ can be written as the smear-smear amplitude A_s, which is a parameter used in the fitting procedure. The other type of smearing used is local-axial, which smears only one component:

$$C_a(t) \approx \frac{Z_s}{2am_\pi} \langle \pi | \mathscr{A}_t | 0 \rangle \, e^{-am_\pi t} = A_a e^{-am_\pi t} \tag{2}$$

where $C_a(t)$ is the local-axial correlator, $\langle \pi | \mathscr{A}_t | 0 \rangle$ is the axial-current matrix element, and $\mathscr{A}_t$ is the axial current $\overline{q}\gamma^5 q$, where $\overline{q}$ is an antiquark, q a quark, and γ^5 represents the product of all gamma matrices. $\langle \pi | \mathscr{A}_t | 0 \rangle$ is a constant proportional to f_π through the relation

$$\langle \pi | \mathscr{A}_t | 0 \rangle = f_\pi^{\text{bare}} m_\pi, \tag{3}$$

where f_π^{bare} is the pion decay constant before renormalization, and m_π is the pion mass.

Because we are ultimately interested in finding $\langle \pi | \mathscr{A}_t | 0 \rangle$, its plots need particular attention. The shape of this plot changes between datasets, as do the others, but is unique because it cannot be found directly from fitting $C_s(t)$ and $C_a(t)$ independently. From Eq. 2 one can see that the ground-state fit will yield am_π and A_a. The constant $\langle \pi | \mathscr{A}_t | 0 \rangle$ can then be solved for if Z_s is known from a fit of $C_s(t)$. This method of finding $\langle \pi | \mathscr{A}_t | 0 \rangle$, referred to as Method I, is compared to another method to determine the most stable approach. Method II requires one fit of a manipulated correlator:

$$\frac{C_a(t)^2}{C_s(t)} \approx \frac{\langle \pi | \mathscr{A}_t | 0 \rangle^2}{2am_\pi} e^{-am_\pi t} = A_r e^{-am_\pi t} \tag{4}$$

where am_π and A_r is the mass and amplitude of the manipulated correlator, respectively. By comparing the $\langle\pi|\mathscr{A}_t|0\rangle$ evolution plots for these two methods we can determine which is better suited for finding the constant. Figure 1 shows a plot of the fitted matrix element as a function of t_{min}, the minimum time used in the fit, for both methods. The manipulated correlator is slightly less stable because it is constantly increasing; for this reason all values of $\langle\pi|\mathscr{A}_t|0\rangle$ were found using Method I.

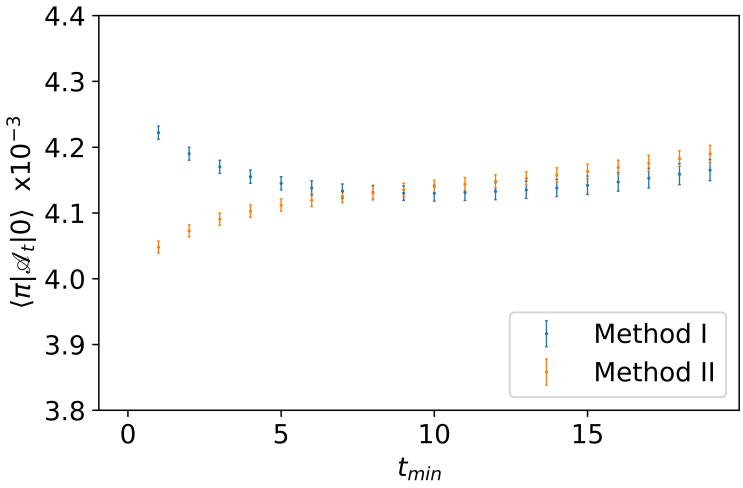

Figure 1. The constant $\langle\pi|\mathscr{A}_t|0\rangle$ as a function of minimum fit time for both fit methods of the a06m310 ensemble. Because the result from Eq. 4 (orange markers) is always increasing, it was deemed less stable than the method requiring a fit of each the $C_s(t)$ and $C_a(t)$ correlators from Eq. 1 and Eq. 2, respectively (blue markers).

The constant $\langle\pi|\mathscr{A}_t|0\rangle$ can be extracted from the correlator data using an uncorrelated ground-state fit. The ground-state fit looks like a single exponential term where the two parameters are the amplitude and energy of the pion at its lowest energy state. Because the lowest-energy state is at rest, the energy parameter is the mass. Therefore, on a plot of effective mass a good correlator fit will also fit the effective-mass plateau, where the pion is at its ground-state energy. The effective mass is given by

$$m_{\text{eff}} = \ln\left(\frac{C(t)}{C(t+1)}\right), \tag{5}$$

where $C(t)$ is any correlator. The effective-mass plot is a valuable tool in fitting the correlator, as it provides easy visualization of the ground state and allows us to easily see whether there is higher-state contamination. We fit jackknifed correlator data to reduce bias. Because we only want to fit the ground state, a minimum and maximum time of the fit needs to be designated so that any points that pull the data away from the ground state are removed. These limits are chosen based on the evolution of the fitting parameters, $\langle\pi|\mathscr{A}_t|0\rangle$, and the $\frac{\chi^2}{\chi^2_{\text{min}}}$ with increasing t_{min} and decreasing

t_{max}, the maximum time used in the fit (Fig. 2). When the higher state is completely removed these evolution plots appear stable, showing little to no change in the magnitude of the parameter with changing t_{max} or t_{min}. The effective-mass plot is also consulted, as there may appear many possible bounds in the evolution plots, the effective mass aids in determining a good fit.

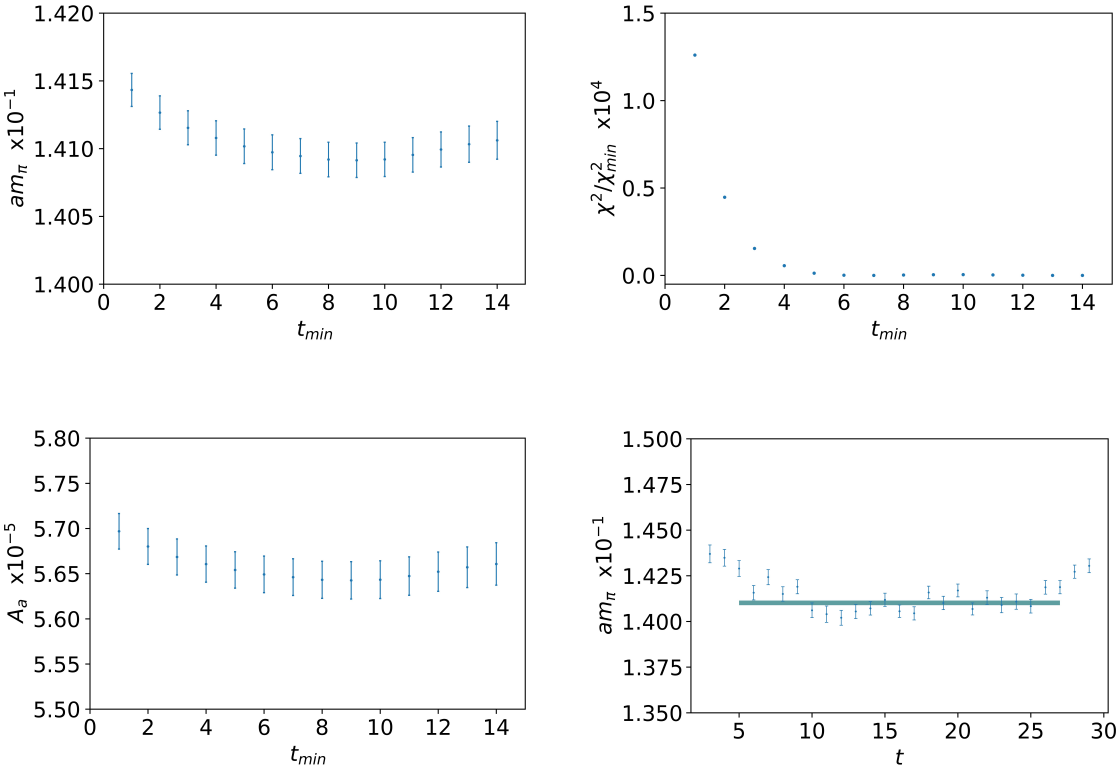

Figure 2. t_{min} evolution plots, and ground-state fit for the a09m310 ensemble. (Top left) Mass parameter in lattice units (am_π) changing with increasing t_{min}. (Top right) Chi squared approaches one as t_{min} increases. (Bottom left) The amplitude evolution with t_{min}. (Bottom right) The correlator fit band shown on the effective-mass plot as a function of time. Uncertainty is given as the width of the band. The minimum time is chosen to be in a region that is relatively stable, for this ensemble $t_{\text{min}} = 5$ to $t_{\text{min}} = 10$ was considered stable, in this case $t_{\text{min}} = 5$ was chosen to fit the most data. t_{max} is determined in a similar manner.

3. RESULTS AND DISCUSSION

The pion mass in lattice units am_π is taken from the effective-mass plot and converted into physical units m_π for use in Eq. 3. The bare pion decay constant f_π^{bare} can then be renormalized to the pion decay constant f_π (Table 1) using a renormalization constant Z_A found in Ref. [3]. The results from the fit of all six ensembles are found in Table 1.

Ensemble	Z_A	a **(fm)**	m_π **(MeV)**	f_π **(MeV)**	$L^3 \times T$
a12m310	0.95(3)	0.1207(11)	311.0(2.9)	93.3(3.5)	$24^3 \times 64$
a12m220	0.95(3)	0.1184(10)	288.5(2.0)	95.8(3.6)	$32^3 \times 64$
a09m310	0.95(4)	0.0888(08)	312.8(2.8)	98.3(4.6)	$32^3 \times 96$
a09m220	0.95(4)	0.0872(07)	226.6(1.8)	95.8(4.4)	$48^3 \times 96$
a09m130	0.95(4)	0.0871(06)	142.5(1.0)	93.9(4.2)	$64^3 \times 96$
a06m310	0.97(3)	0.0582(04)	319.5(2.2)	101.9(3.5)	$48^3 \times 144$

Table 1. The renormalization constant Z_A and lattice spacing a for each ensemble [3], along with the fit results for pion mass m_π and decay constant f_π with their respective statistical errors. The far right column labels the lattice sizes along the spatial (L) and temporal (T) directions.

The results from the correlator fits cannot yet be compared to the physical value because of the non-physical assumptions made during the lattice calculation. The lattice spacing and pion mass must be extrapolated to their physical values. Using the fit function [3, 4]:

$$f(a, m_\pi) = C_0 + C_a a + C_m m_\pi^2, \tag{6}$$

the correlator results can be fit to a plane and the physical value interpreted from this relationship. The f_π mean and error associated with every ensemble are recreated using the jackknife mean and variance of a randomly generated gaussian distribution. The jackknife samples are then fit with Eq. 6 and extrapolated to $m_\pi = 139.57061(24)$ [5], and $a = 0$. The pion mass and error from Ref. [5] were also reconstructed for calculation using gaussian sampling.

The extrapolation is viewed as cross sections through a three-dimensional plot so that the dependence of f_π on a and m_π can be viewed independently (Fig.3). When extrapolated to the physical point the fit of the ensemble data (Table 1) to Eq. 6 yields a value of $f_\pi = 103.5(4.5)$ MeV.

Compared to the accepted experimental value of 89.80 (1)(9), the errors come from the experimental rate measurement and the radiative correction factor, respectively [5], our value is slightly large. The difference is less substantial when compered to other lattice calculations such as the value found in Ref. [3] of approximately 95 MeV. This may be the result of higher-state contamination left over from the correlator fit. The ground-state fit exposes the mass to the possibility of higher-state influence. Although the fitting procedure aims to fit only the effective-mass plateau, the possibility of higher-state influence is not completely eliminated, as the plateau is not always clearly defined. In

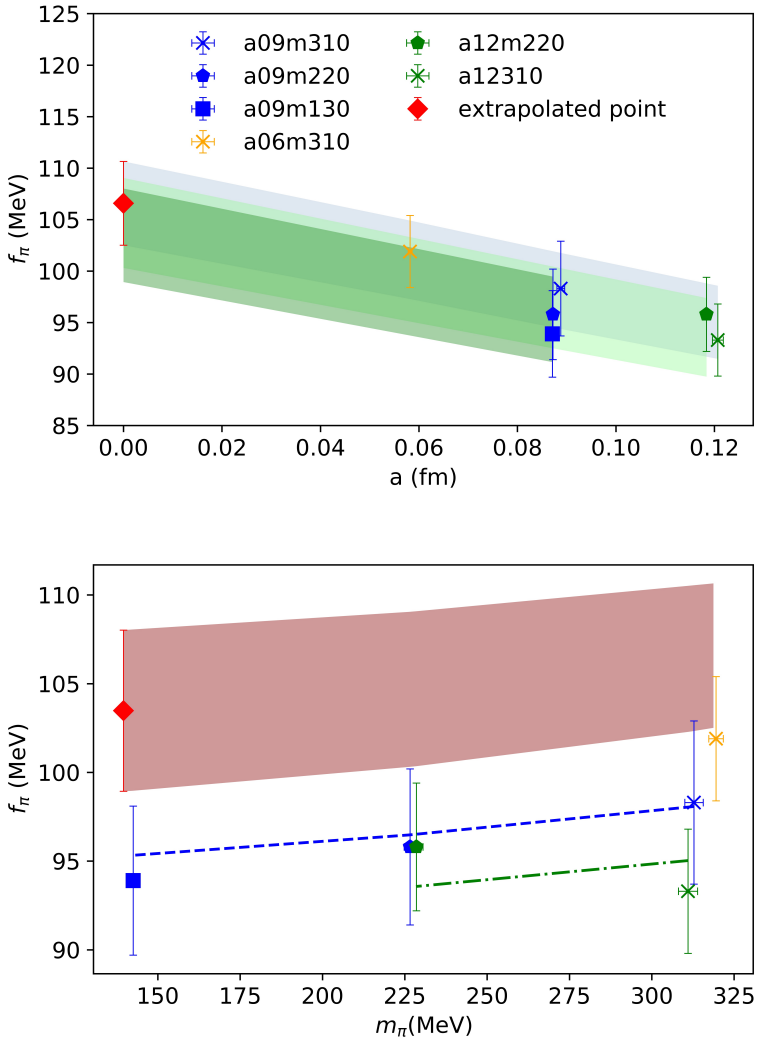

Figure 3. (Top) Final decay-constant fits for all three masses when extrapolated to the continuum limit as a function of lattice spacing. This is a slice along the mass domain of the three-dimensional plot generated from Eq. 6. The masses are distinguished by the marker shape, while the lattice spacing by marker color. The red marker is the value of f_π at the continuum. The trend shows that f_π decreases with increasing a. The dependence of f_π on the mass is also visible by the stacking of the fit bands, greater mass yields a greater f_π. These relationships are again confirmed when observing f_π versus m_π (bottom), which is a slice along the lattice-spacing domain. It is obvious that f_π depends heavily on a.

future work, contamination could be eliminated by using a higher-state fit, accomplished by adding another exponential term onto the fit function. By including the higher-energy states, there is less chance of outside contamination during the fit. This analysis also provides values for C_a, C_m, and the chiral limit C_0 (Table 2). These constants provide additional insight into quark behavior.

	Fit Results	**Units**
C_0	102.7 (4.7)	MeV
C_a	–94.2 (3.9)	MeV $\cdot$ fm^{-1}
C_m	$3.78(0.64) \times 10^{-5}$	MeV^{-1}
f_π	103.5 (4.5)	MeV

Table 2. Results from the fit of ensemble data using Eq. 6, where C_0, C_a, and C_m are all constants, and C_0 is the chiral limit.

4. CONCLUSIONS

The pion decay constant provides insight into the ability of QCD to explain physics at the femtoscale (10^{-15} m). In this analysis f_π is determined from lattice-QCD ensembles generated by the MILC collaboration [2]. The value for f_π without QED correction is $f_\pi = 103.5(4.5)$ MeV, considering only statistical errors. This is slightly higher than [3, 5] which yield a value of approximately 95 MeV and 89.80 (1)(9) MeV, respectively. Future work may investigate the influence of the higher-energy states in the data. Additionally, this work could be expanded to approximate the value of the weak mixing matrix element V_{us}, providing further insight into the accuracy of QCD.

5. ACKNOWLEDGMENTS

I owe a special thanks to Professor Huey-Wen Lin, Zhouyou Fan, Rui Zhang, Ruizi Li, and Kuan-Yu Lin of Michigan State University Department of Physics and Astronomy for their guidance throughout this work. This material is based upon work supported by the National Science Foundation (NSF) under Grant No. 1559866. This work is in contribution to CAREER: Constraining Parton Distribution Functions for New Physics Searches, NSF Grant No. 1653405.

References

[1] R. Gupta, Introduction to lattice QCD: Course, arXiv:hep-lat/9807028v1
[2] A. Bazavov et al. (MILC Collaboration), Phys.Rev. D87, 054505 (2013), arXiv:1212.4768 [hep-lat].
[3] Battacharya et al. (PNDME Collaboration), Phys.Rev. D94, 054508 (2016), arXiv:1606.07049v3[hep-lat].
[4] The Flavor Lattice Averaging Group (FLAG), (2019), arXiv:1902.08191v2[hep-lat].
[5] M. Tanabashi et al. (Particle Data Group). Phys.Rev. D98, 030001 (2018) and 2019 update.

STUDENT JOURNAL OF PHYSICS

Effect of size and shape on the melting point and volume thermal expansion of Nano-Germanium

Pratyay Chattopadhyay

Second year M.Sc., Department of Physics and Electronics, St. Xavier's College (Autonomous)
Ahmedabad-380009
Email-:pratyay10@gmail.com

Date Received: 31/Jan/2020 **Date Published: 21/Aug/2020**

Abstract-: Germanium is a semiconductor with vivid applications in the field of nanoscience and other lines of physics. With having known information about the bulk characteristic of germanium, an effort has been made to investigate the characteristics of germanium when it is in nanoscale. In the present work effect of size and shape on the melting point and volume thermal expansion of nano-germanium has been studied.
Keywords: Nano-particles, Melting point, Nano-germanium

1. INTRODUCTION

In the present paper a study of the effect of shape and size on the thermodynamical properties of nanomaterials has been carried out. Nanomaterials are the materials having size ranging from 1 to 100 nanometers (10^{-9}meters). Nanomaterials are of current interest because they show noble physical and mechanical properties that may differ from that of their corresponding bulk materials [1,2].

The use of nanomaterials is vast and has got many real life applications [3]. Nanomaterials are mostly used in healthcare products, paints, manufacturing processes. In the field of medicine enzymes of the size of nanometers, called nanozymes, are used to do or copy the exact work of an enzyme. Apart from being used as nanozyme, they are also used in bioimaging, biosensing and many more. They are also used in paints for UV protection. Many high quality and advanced filters are being made which are capable of removing particulate as small as viruses from water. There are many other applications in daily human life and some are still yet to be discovered.

The effect of size on the thermodynamic properties of any nanomaterials is quite intense. As the size reduces the surface to volume ratio increases drastically. The change in the surface to volume ratio changes the physical properties of the material and the effect of quantum confinement is also observed. The effect of size and shape on the thermodynamic properties plays very important role to understand the physics of the nanomaterials. In the following section a theoretical method has been discussed to study the dependency of melting point and coefficient of volume thermal expansion on the size and shape of nanomaterials.

2. METHODOLOGY

The variation in the melting point against the size of nanosolids can be understood using W.H.Qi model [4]. Qi proposed a model to compute the melting temperature, based on the cohesive energy of nanosolids. The cohesive energy formula reads as follows

$$E_p = E_b\left(1 - \frac{N}{2n}\right) \quad (1)$$

Where E_p and E_b are the cohesive energy of nanosolid and corresponding bulk material. Here n and N are the total number of atoms of a nanosolid and total surface atoms respectively.

From the above relation of cohesive energy we can directly write the expression of melting temperature because there is a linear relation among them [4]. Accordingly the melting temperature can be written as follows-:

$$T_{(mp)} = T_{(mb)}\left(1 - \frac{N}{2n}\right) \quad (2)$$

Where $T_{(mp)}$ and $T_{(mb)}$ are the melting temperatures of nanosolid and corresponding bulk material.

To calculate $T_{(mp)}$ we have to first calculate the value of ratio N/n. The values of this ratio depend upon the shape and size of the nanosolids. In the present work, an attempt has been made to compute the ratio N/n for nanosolids namely spherical nanoparticles, nanowires and nanofilms.

To investigate for spherical nanoparticles let the diameter of the particle be D, then the volume is given by $[\pi D^3/6]$. If d be the diameter of the atom, then the volume of each atom is given by $[\pi d^3/6]$.

Hence the total number of atom n is given by $n = [(\pi D^3/6) / (\pi d^3/6)]$, which on further simplification gives us the value of $n = [D^3/d^3]$. Hence number of interior atoms is n-N. We know that the surface area of the nanosolid can be written as $[\pi D^2]$, and the contribution of each surface atom is $[\pi d^2/4]$. Hence the total number of surface atoms is the ratio of the surface area of the nanosolid to the surface area of the atom, i.e. $N = 4\,D^2/d^2$. Thus for the spherical nano-particle the ratio of N/n is (4d/D).

Similarly the values of ratio N/n for nanowires and nanofilms can be computed [4] and their values are tabulated in the Table-1[4].

Nanosolid	N/n
Nanosphere	4d/D
Nanowire	(8/3)d/l
Nanofilm	(4/3)d/h

Table-1-: Calculated value of the ratio of N/n for three different types of nanosolids. For the disk like nanosolid l and h are the diameter of nano wire and width of nano film.

The change in dimensions of a material, when either heated or cooled, is linearly related to the change in temperature. Coefficient of volume thermal expansion α is defined as follows,

$$\alpha = \frac{1}{V}\left(\frac{\partial V}{\partial T}\right)_P \tag{3}$$

R. Kumar *et al.*[5] determined the value of coefficient of volume thermal expansion using eq (3) and proposed the following relation of coefficient of volume thermal expansion for nanosolids

$$\alpha = \alpha_{(b)}\left(1 - \frac{N}{2n}\right)^{(-1)} \tag{4}$$

Where $\alpha_{(b)}$ is the coefficient of volume expansion for bulk material.

3. RESULTS AND DISCUSSION

Using eq (2) the melting temperature for nano-germanium has been computed and our predicted results for spherical nanosolids, nanowires and nanofilms are reported in Fig-1. The predicted results are reported for the particle size up to 13 nm. The results of the melting temperature for particles having size above 13 nm are similar to their corresponding bulk counterparts.

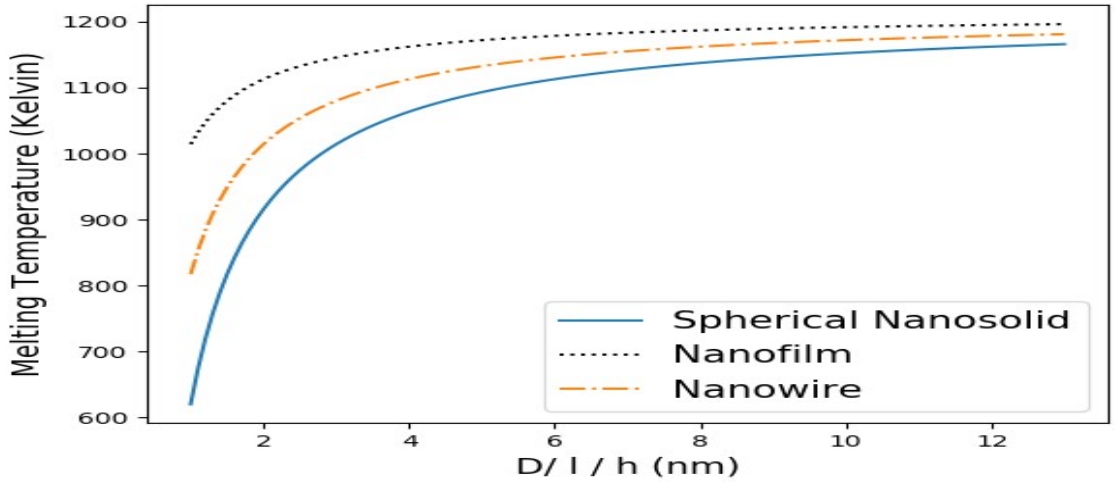

Fig-1 Size dependence of melting temperature of nanogermanium

It is observed that melting temperature decreases with decreasing size, irrespective of the shape of the nanosolids. A sharp decrease in the melting temperature is observed below the size 6nm for all the shapes of nanosolids. At nano-level the surface to volume ratio increases drastically and the thermodynamic and thermal properties get altered. Having high surface to volume ratio the atoms are readily available at the surface, which are loosely bound in comparison to their bulk equivalent. The heat distribution is even and speedy due to which the molecules melt faster compared to their bulk counterparts. This is how the size plays a major role in determining the melting temperature of nanosolids. Nevertheless, the effect of shape of a nanosolid also has a high impact on the melting temperature and we found that it is more for spherical nanosolid followed by nanowire and nanofilm.

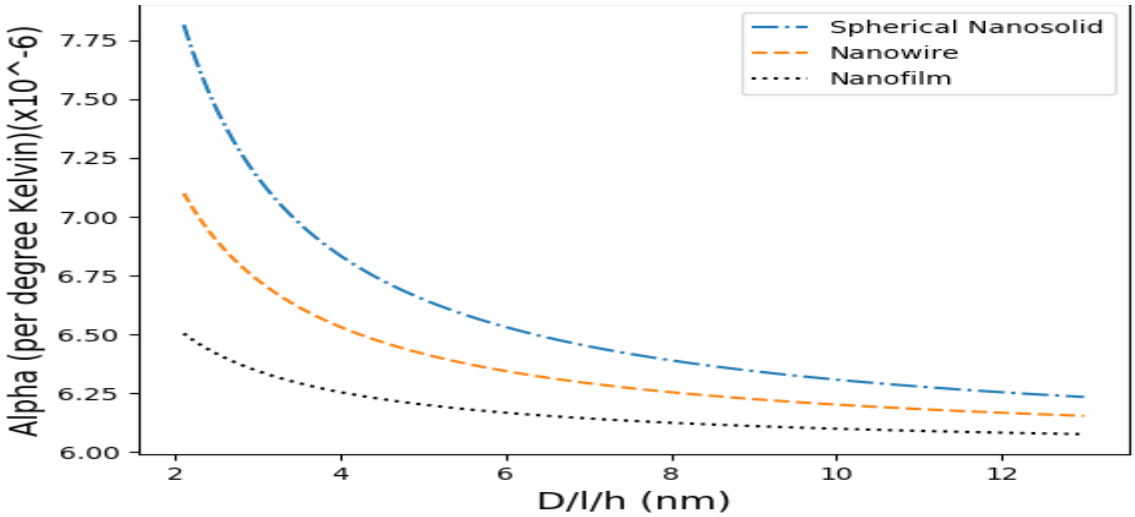

Fig-2 Size dependence of coefficient of volume thermal expansion of nano germanium

Using eq (4) the coefficient of volume thermal expansion for nano-germanium has been calculated. The comparative study of variation of volume thermal expansion of germanium spherical nanosolid, nanowire and nanofilm is reported in fig-2. From the results it is noted that variation in coefficient of volume thermal expansion is significant when the size of the nanosolid is less than 10 nm. It is found that the variation of volume thermal expansion for spherical nanoparticles is more compared to nanowires and nanofilms. It is observed that the coefficient of volume thermal expansion increases as the size of nanosolids decreases. We are reporting our predicted results of melting temperature and coefficient of volume thermal expansion for nanogermanium in the absence of experimental data. These predictions may be of current interest to the researchers engaged in the experimental studies.

EFFECT OF VOID SPACE ON N/n

In order to calculate the number of atoms inside a spherical nanoparticle of diameter D using a hard sphere model for the atoms of diameter d, one has to know the empty space between atoms when they are densely packed. This is a nontrivial problem. We will use a simple model to estimate the volume of this void space/atom using a cubic nanoparticle of cube length D inside which the atoms are arranged in a cubic lattice and use this value for the spherical nanoparticle. This should be reasonable when D >>d.

Inside a cube of length D (volume D^3), we can tightly pack $N_0 = (D/d)^3$ atoms. The volume occupied by the atoms is $V_{atom} = N_0$ □ $V_{atom} = N_0 (\pi/6)d^3$. The volume of the empty space per atom then $V_{void} = [(D^3 - V_{atom}) / N_0] = [1- (\pi/6)] d^3$. Using this we estimate the number of atoms inside the spherical nanoparticle as $n = [\pi/6 (D/d)^3] < N_0$.

Using similar idea we estimate the number of atoms at the surface (N) of the spherical nanoparticle. We take a shell at the surface of volume $V_{surf} = 4\pi(D/2)^2 d$ and obtain the inequality

$$\frac{V_{surf} - V_{void}}{V_{atom}} < N < \frac{V_{surf}}{V_{atom}} \qquad (5)$$

This reduces to:

$$\pi\left(\frac{D}{d}\right)^2 < N < 6\left(\frac{D}{d}\right)^2 \qquad (6)$$

If we use a naïve model where we take the surface area of the nanoparticle [πD^2] and divide it by the cross sectional area of an atom [$\pi d^2/4$], we get N = [4 $(D/d)^2$] which satisfies the above inequality and closure to the value which allows for the void space correction, not bad.

$$\frac{N}{n} = \pi\left(\frac{D}{d}\right)^2 \times \left(\frac{6d^3}{\pi D^3}\right) = \frac{6d}{D} \qquad (7)$$

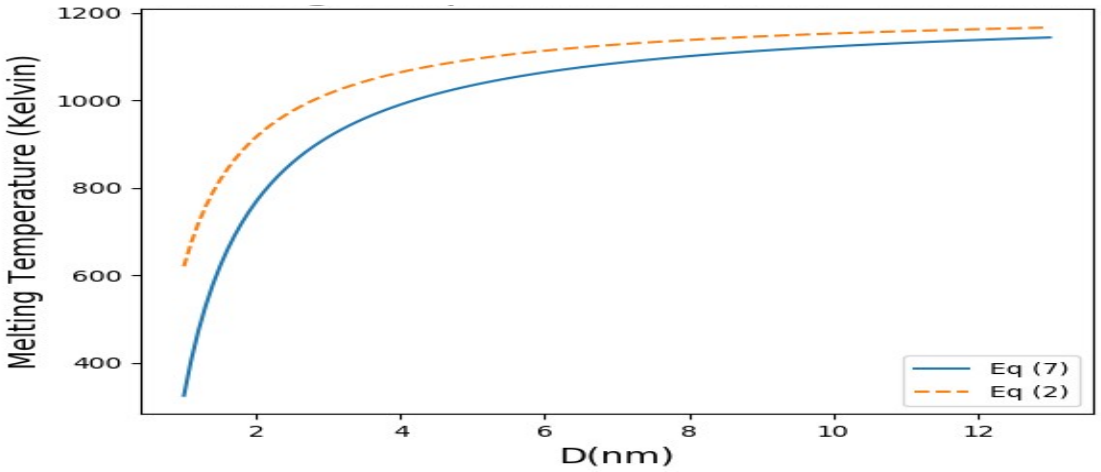

Fig 3-: Size dependence of melting temperature of nanogermanium

The ratio is 3/2 times larger than that obtained by the simple model used earlier 4d/D. Using eq (7) we have calculated the melting temperature and coefficient of volume thermal expansion of nano germanium for spherical nanoparticle and the predicted results are shown in fig 3 and fig 4.

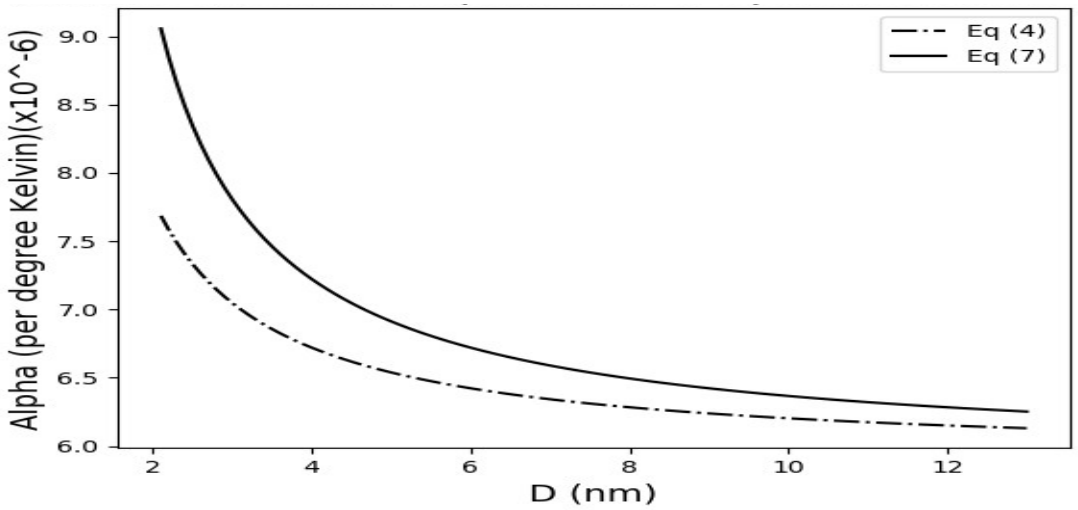

Fig 4-: Size dependence of coefficient of volume thermal expansion of nano germanium

We have found that the results of melting temperature computed considering the void space correction are 0.66 times less than the results obtained by the Qi model. Predictions of coefficient of volume thermal expansion considering the effect of void space may be of current interest to the researchers engaged in the experimental studies.

CONCLUSION

In the present work the effect of size and shape on the melting temperature and co-efficient of volume thermal expansion of the nanocrystalline germanium has been studied. The model predicts that the melting temperature decreases as the size of particles decreases, irrespective of the shape of the nanosolids. We have found that the co-efficient of volume thermal expansion increases as the particle size decreases. It is found that the particle shape have large effect on small particle than on large particle which indicates that the particle shape should be taken in to consideration in the study of thermal properties of nanoparticles in small size. The present approach for melting temperature and co-efficient of volume thermal expansion may be used to understand behaviour of nanosolids.

ACKNOWLEDGEMENT

I am thankful to St. Xavier's College Ahmedabad for giving me an opportunity to do project work in the field of Physics and helping me to pursue my research dream. I express my sincere gratitude to Principal Father (Dr.) Lancelot D' Cruze, Vice-Principal Father Johnson for letting me use the resources of St. Xavier's College. Thanks to Dr. Tushar Pandya, department of Physics, St. Xavier's College, for helping me in this project. I want to thank the referee Emeritus Professor S.D. Mahanti for his valuable comments and kind cooperation.

REFERENCES

1. A. D. Cicco, A. C. Frasini, M. Minicucci, *et al.* Structure of crystalline and amorphous Ge probed by X-ray absorption and diffraction techniques, Phys. Stat. Sol. B, 240; 19(2003)
2. J. Crain, G.J. Ackland and S.J.Clark; Exotic structures of tetrahedral semiconductors, Rep. Prog. Phys., 58; 705(1995)
3. W. J. Stark, P. R. Stoessel, W. Wohlleben *et al.* Industrial applications of nanoparticles, Chem. Soc. Rev.**,** 44**;** 5793(2015)
4. W. H. Qi , Size effect on melting temperature of nanosolid, Physica B Condensed Matter 368(s 1– 4):46–50(2005)
5. Raghuvesh Kumar, Geeta Sharma and Munish Kumar, Size and Temperature Effect On Thermal Expansion Coefficient And Lattice Parameter Of Nanomaterials, Modern Physics Letters B, Vol. 27, No. 25, 1350180 (2013)

Effects of structural properties on Hydrogen Storage capacity of multi-element AB_5-type Hydrogen Storage alloy

Sapna Prajapati, Kuldeep Panwar and Sumita Srivastava

M.Sc. III Semester

Department of Physics, Pt. L.M.S. Government Post Graduate College, Rishikesh

(Autonomous College) Dehradun-249201, India

Email: sapnaprajapati96@gmail.com

Date Received: 31/Jan/2020 Date Published: 21/Aug/2020

Abstract: In this work a relation has been established for harnessing hydrogen as renewable energy source, storage of hydrogen is the key factor. Solid state hydrogen storage is the safest method among all the methods. Hydrogen storage capacity is an important parameter for application point of view. The various substitutions and tailoring in the parent alloy may change the storage capacity for specific application. In present investigation, experimentally observed values of hydrogen storage capacity reported in literature have been correlated with the structural properties of hydrogen storage alloys. Some of the structural properties like lattice parameters, unit cell volume , void size have been noted from reported values in literature, while other structural properties like equivalent radius r_B*, ratio of r_A/r_B* and contraction in A-B bond have been calculated in present study. The effects of these structural properties on multi-element AB_5-type hydrogen storage alloys have been studied in the present work.

Keywords: Hydrogen storage alloys, Hydrogen absorption

1. INTRODUCTION

Hydrogen storage alloys are characterized by several properties, like, hydrogen storage capacity, hydrogen absorption/desorption plateau pressure, kinetics, heat of formation etc. In storage applications like, vehicles, Ni-MH battery, stationary storage, hydrogen storage capacity is the most important property [1, 2]. Hydrogen storage alloys are materials, which absorb hydrogen at certain pressure and desorb it at lower pressure. Hydrogen atom is stored in the solid material at interstitial position. State of the art hydrogen storage alloys are AB_5, AB_2, A_2B and AB type. Among so many hydrides, AB_5 is popular for its easy activation and operation at room temperature and at little atmospheric pressure [1-4]. Tailoring in the hydrogen storage alloy may be achieved either by adopting different synthesis route or through substitution of other elements in the parent alloy either at 'A' or at 'B'. For specific requirements of hydrogenation properties, multi-element compositions are preferred over binary compound of AB_5. At present no model is available, which can predict the hydrogen storage capacity of multi-element alloy before synthesis.

To understand the ability of hydrogen storage, it is important to discuss the structure of alloy. In present study, AB_5-type alloy has been chosen to demonstrate the structural model. AB_5-type intermetallic corresponds to $CaCu_5$-type structure with hexagonal Unit and space group P6/mmm [5]. There is one AB_5 unit per unit cell. Conditions for ideal packing are:

$$c = (\sqrt{2}/\sqrt{3})\ a \text{.....(1)}$$

$$R_B = a/4 \text{.....(2)}$$

$$R_A = (a/\sqrt{3}) - (a/4) \text{.....(3)}$$

Where a, c = lattice parameters and R_A , R_B = Atomic radius

There are in total 34 tetrahedral holes in one AB_5 unit. But all the holes cannot be occupied simultaneously due to stability consideration. One famous rule known as Switendic Criterion states that minimum distance between two H atoms is 2.1Å [6]. Radius of voids can be calculated as under [7].

Type II AB_3 tetrahedral hole (H_I site) = R_A = 0.075459a .....(4)

Type I AB_3 tetrahedral hole (H_{II} site) = R_A = 0.076365a .....(5)

The atomic radius of substituted element in the parent alloy may play an important role. However equivalent radius calculated in the present study for the alloy without synthesis also seems to be equally important. The effect of structural properties has been studied on three alloy hydride series. In earlier studies, theoretical approach for explaining thermodynamic properties has been presented [5-8], but no report is available on correlation of structural properties with hydrogen storage capacity. In this work, a relation has been established between structural properties and hydrogen storage property.

2. METHODOLOGY

In present investigation, three series of alloys have been studied. These alloys series are termed as alloy1, alloy2 and alloy3. The nomenclature of alloys is given in Table 1. For each alloy series, experimentally observed values of lattice parameters ‘a’ and ‘c’ along with hydrogen storage capacity reported in literature have been noted. Equivalent radius r_B* has been calculated in present study by taking stoichiometric composition of various elements at ‘B’ and atomic radius of each element. The values of atomic radius for element under present study are given in Table 2. The ratio of r_A/ r_B* and contraction in A-B bond has been calculated in the present study. Contraction in A-B bond has been calculated as given below:

$$\text{Contraction} = (r_A + r_B^*) - (r_{A\text{-}B}) \text{.....(6)}$$

$$\text{Where, } (r_{A\text{-}B}) = a/\sqrt{3} \text{.....(7)}$$

Graphs have been plotted among structural properties and hydrogen storage capacity for each alloy and a relation has been established.

Table 1- Nomenclature of alloys

S.N.	**Name of alloy**	**Composition of alloy**
1	Alloy 1	$LaNi_4R$ (R= Al, Mn, Fe, Cu, Co, Cr)
2	Alloy 2	$LaNi_{5-x-y-z}Al_xSn_yFe_z$
3	Alloy 3	$La_{0.78}Ce_{0.22}Ni_{3.73}Co_{0.30}Al_{0.1}7Fe_{0.5-x}Si_x$ (x = 0, 0.05, 0.075, 0.1)

Table 2- Atomic radius of elements using VWR Sargent Welch Periodic Table

S.N.	Element	Atomic Radius **(Å)**
1	La	2.74
2	Ce	2.70
3	Ni	1.62
4	Co	1.67
5	Mn	1.79
6	Fe	1.72
7	Si	1.46
8	Al	1.82
9	Cu	1.57
10	Cr	1.85

3. RESULTS AND DISCUSSIONS

Table 3 shows all the known and calculated parameters of alloy 1-$LaNi_4R$ hydride.

Table 3- Known and calculated parameters of alloy 1 $LaNi_4R$ hydride [9,10]

S.N.	Alloy	a (Å)	c (Å)	Unit Cell Volume ($Å^3$)	r_B^* (Å)	r_A/r_B^*	Contra-ction in A-B Bond (Å)	Void size H_I (Å)	Void size H_{II} (Å)	Hydrogen Storage Capacity (H/M)
1	$LaNi_5$	5.017	3.986	86.28	1.62	1.691	1.46	0.37858	0.38312	6
2	$LaNi_4Co$	5.018	3.981	86.2	1.63	1.681	1.473	0.37865	0.3832	4
3	$LaNi_4Cu$	5.033	4.007	87.29	1.61	1.702	1.44	0.37979	0.38435	5
4	$LaNi_4Fe$	5.049	4.015	88.02	1.64	1.671	1.46	0.38099	0.38557	5
5	$LaNi_4Cr$	5.07	4.048	90.23	1.666	1.645	1.479	0.38258	0.38717	4
6	$LaNi_4Mn$	5.089	4.082	90.91	1.654	1.657	1.454	0.38401	0.38862	6
7	$LaNi_4Al$	5.061	4.07	89.65	1.66	1.651	1.478	0.3819	0.38648	4.5

Table 3 shows that, in most of the cases hydrogen storage capacity decreases with increasing value of lattice parameter, unit cell volume, void size, r_B^* and contraction in A-B bond. r_A/r_B^* shows opposite effect on hydrogen storage capacity. It may be mentioned here, that in $LaNi_4R$ hydride series, all of the substituted elements belongs to transition element except Al. Electronic properties of transition elements also affect the hydrogen storage capacity. But the effect of electronic property on hydrogen storage capacity has not been studied in the present investigation. The deviation in the trend may be due to negligence of electronic property. The trend in hydrogen storage capacity is similar with unit cell volume, void size and r_B^*. It may be mentioned here, that unit cell volume is experimental value noted after synthesis of alloy, whereas r_B^* is calculated value found without synthesis of alloy. In this way, r_B^* is playing the same role as unit cell volume. Hence by calculating the value of r_B^*, one can predict the trend of hydrogen storage capacity without synthesis of the actual alloy.

Similarly known and calculated parameters of Alloy 2:$LaNi_{5-x-y-z}Al_xSn_yFe_z$ hydride are shown in Table 4. This table shows no clear trend in variation of hydrogen storage capacity with lattice parameters, unit cell volume and void size. However a clear trend in storage capacity has been observed with r_B^*, r_A/r_B^* and Contraction in A-B bond. Hydrogen storage capacity decreases with increasing values of r_B^*, r_A/r_B^* and Contraction in A-B bond. Figures1 and 2 show variation in storage capacity with unit cell volume and r_B^* respectively.

Table 4- known and calculated parameters of Alloy 2:$LaNi_{5-x-y-z}Al_xSn_yFe_z$ hydride [11]

S.N.	Alloy	a (Å)	c (Å)	Unit Cell Volume ($Å^3$)	Void size H_I (Å)	r_B^* (Å)	r_A/r_B^*	Contr-action in A-B bond (Å)	Hydroge n Storage Capacity (H/M)
1	$LaNi_5$	5.1037	3.8936	84.1717	0.3783	1.62	1.6914	1.465	6.43
2	$LaNi_{4.8}Sn_{0.1}Al_{0.1}$	5.0295	3.9987	86.9895	0.3795	1.623	1.6884	1.459	6.45
3	$LaNi_{4.6}Fe_{0.2}Al_{0.2}$	5.0307	3.9997	87.0527	0.3796	1.632	1.6789	1.467	6.3
4	$LaNi_{4.8}Sn_{0.2}$	5.0332	4.0107	87.3789	0.3798	1.621	1.6905	1.455	6.67
5	$LaNi_{4.6}Sn_{0.2}Fe_{0.2}$	5.0403	4.0052	87.5055	0.3803	1.628	1.683	1.458	6.37

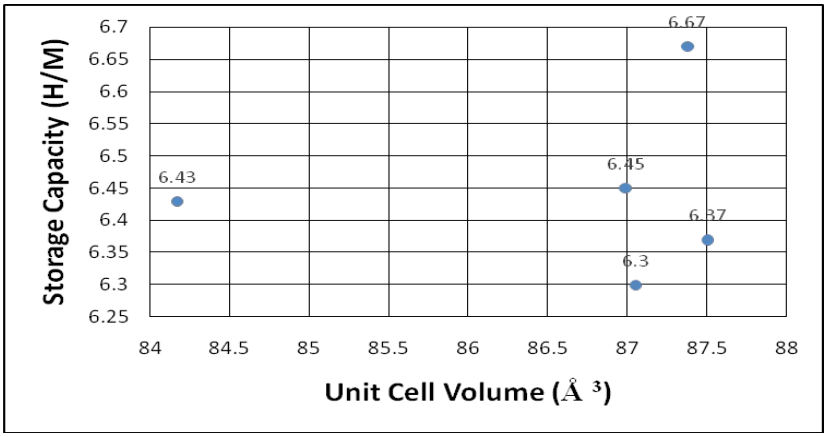

Figure 1- Variation in hydrogen storage capacity with unit cell volume for alloy 2.

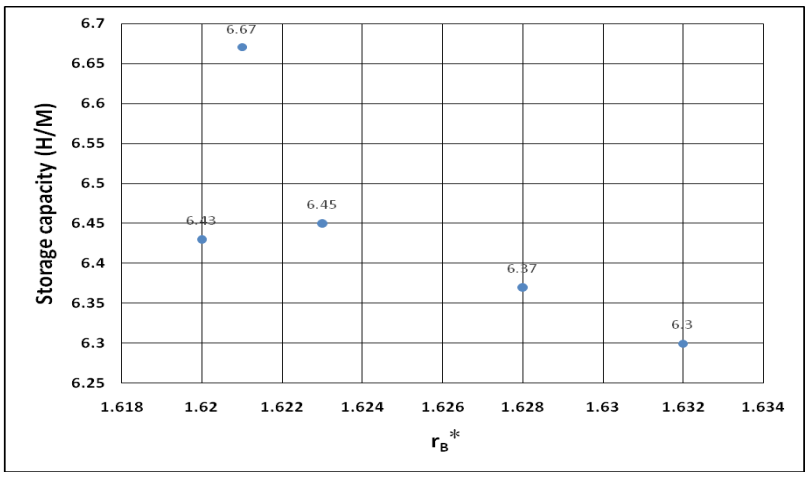

Figure 2- Variation of hydrogen storage capacity with r_B*for alloy 2.

Table 5 shows same data for alloy3: $La_{0.78}Ce_{0.22}Ni_{3.73}Co_{0.30}Mn_{0.30}Al_{0.17}Fe_{0.5-x}Si_x$ multi-element hydride. In this case, hydrogen capacity increases with increasing values of lattice parameters and unit cell volume. However, a decrease in storage capacity has been noted with increasing value of r_B^* and contraction in A-B bond. The variation in storage capacity with unit cell volume and r_B^* is presented in Figures 3 and 4.

Table 5- known and calculated parameters of Alloy 3: $La_{0.78}Ce_{0.22}Ni_{3.73}Co_{0.30}Mn_{0.30}Al_{0.17}Fe_{0.5-x}Si_x$ multi-element hydride [12]

S.N.	Alloy with x	a (Å)	c (Å)	unit cell volume ($Å^3$)	Void Size H_I (Å)	r_B^* (Å)	r_A/r_B^*	Contr-action in A-B bond (Å)	Hydrogen Storage Capacity (H/M)
1	0	5.03	4.045	88.0142	0.37956	1.65	1.6553	1.477	4.85
2	0.05	5.03	4.046	88.0359	0.37956	1.647	1.6579	1.474	5.03
3	0.075	5.031	4.05	88.158	0.37963	1.646	1.6592	1.473	5.06
4	0.1	5.035	4.048	88.2547	0.37994	1.639	1.6669	1.463	5.1

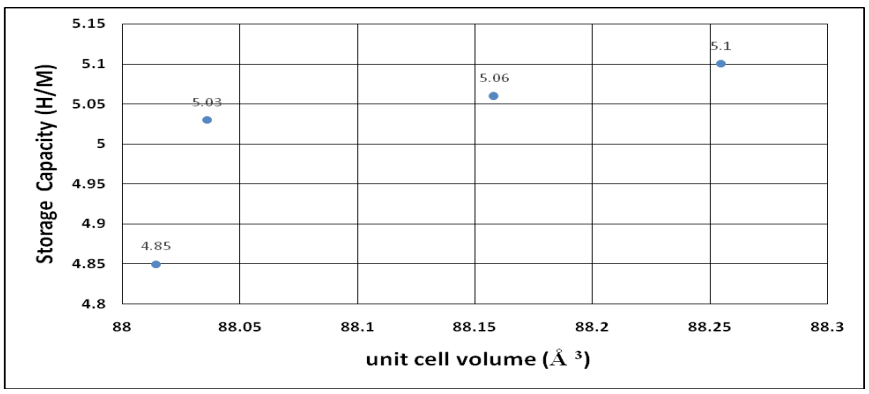

Figure 3- variation of hydrogen storage capacity with unit cell volume for alloy 3.

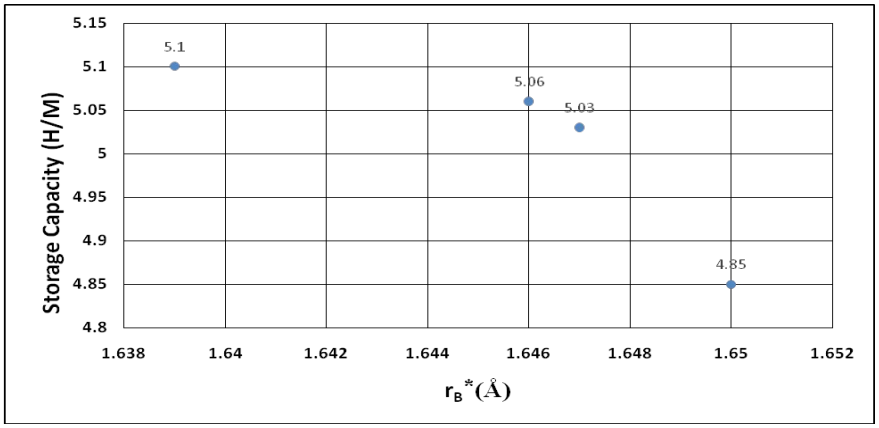

Figure 4- variation of hydrogen storage capacity with r_B^* for alloy 3.

4. CONCLUSIONS

From above discussion, it may be concluded that hydrogen storage capacity decreases with increasing value of r_B*in all the three alloys under study. It may also be concluded that r_B*, r_A/r_B* and contraction in A-B bond are more correct value in comprison to lattice parameters and unit cell volume for prediction of storage capacity. Since unit cell volume is the experimental value, structural parameter r_B^* may be used for predicting hydrogen storage capacity without synthesis of the alloy.

ACKNOWLEDGEMENT

The first author acknowledges support of the Department of Physics, Pt. Lalit Mohan Sharma Government Post-Graduate College, Rishikesh.

REFERENCES

1. Srivastava S, Srivastava ON. Investigations of synthesis and characterization of $MmNi_{4.3}Al_{0.3}Mn_{0.4}$ and $MmNi_{4.0}Al_{0.3}Mn_{0.4}Si_{0.3}$hydrogen storage materials through thermal and spin melting process. Int J Hydrogen Energy 1998; 23:7-13.
2. Srivastava S and Upadhyay RK. Investigations of AB_5-type negative electrode for nickel-metal hydride cell with regard to electrochemical and microstructural characteristics. J Power Sources 2010;195:2996-3001
3. Nagpal M, Kakkar R. An evolving energy solution: Intermediate hydrogen storage. Int J Hydrogen Energy 2018; 43:12168-88.
4. Colbe JB et al. Application of hydrides in hydrogen storage and compression: Achievements, outlook and perspectives. Int J Hydrogen Energy 2019; 44:7780-808.
5. Magee CB, Liu J, Lundin CE. Relationships between intermetallic compound structure and hydride formation. J less common met 1981;78:119-38.
6. Yoshikawa A, Matsumoto T, Yagisawa K. Relationships between crystal structure and Plateau length of pressure-composition isotherms of AB_5 hydrides. J less common met 1982;88:73-79.
7. Van Mal HH, Buschow KHJ, Miedema AR. Hydrogen absorption in $LaNi_5$ and related compounds: experimental observations and their explanation. J less common met 1974; 35:65-76.
8. Lundin CE, Lynch FE, Magee CB. A correlation between the interstitial hole sizes in intermetallic compounds and the thermodynamic properties of the hydrides formed from those compounds. J less common met 1977;56:19-37.
9. Wang FD. Computational modeling of high performance nickel-metal hydride battery materials (2016). Wayne State University Dissertation paper 1494, P 58.

10. Pasturel A, Colinet CC, PercheronGuegan A, Achard JC. Thermodynamic properties of $LaNi_4M$ compounds and their related hydrides. J less common met 1982; 84:73-8.
11. Kazakov AN, Dunikov DO, Mitrokhin SV. AB_5-type intermetallic compounds for biohydrogen purification and storage. Int J Hydrogen Energy 2016;41:21774-79.
12. Zhou W, Wang Q, Zhu D, Wu C, Huang L, Ma Z, Tang Z, Chen Y. The high-temperature performance of low-cost La-Ni-Fe based hydrogen storage alloys with Si substituting. Int J Hydrogen Energy 2016;41:14852-63.

Graphene as high-performance electrodes for GaN nanorod array LED

Ellina Zhang, 11th Grade, Saint Theresa of Lisieux *CHS, Richmond Hill, Ontario L4C 0E8, Canada*

Date Received: 6/Apr/2020 Date Published: 21/Aug/2020

Abstract: Light emitting diodes (LEDs) are an important part of our daily life, accounting for the majority of the world's light source. Thus, the improvement of the efficiency of LEDs is essential. The original GaN nanowire LED with an ITO (indium tin oxide) electrode layer is more efficient than the traditional thin film. However, this efficiency can be increased with the use of monolayer graphene as the electrode. Graphene's low resistivity decreases the operational temperature of the LED device. This allows for more light to be generated at a given temperature and for a smaller decrease in light intensity generated per degree of increase in temperature. In this paper we report a systematic study of the characteristics of graphene as a transparent current spreading layer in GaN nanorod LED. Our experimental results are analyzed in terms of the importance of Shockley-Read-Hall, radiative, and Auger recombination rates occurring in each device. Data for graphene, ITO and the normal thin films are graphed, modeled, and compared with an ABC model, demonstrating a significant increase in IQE (internal quantum efficiency) from the ITO to the graphene device.

Keywords: LED, GaN nanorod array, Graphene electrode

1. INTRODUCTION

Light-Emitting Diodes (LEDs) have become an important light source due to their increased efficiency over fluorescent and incandescent light bulbs. LEDs are devices constructed from the combination of semiconductors. Going back to the basics, a semiconductor is a material whose conductivity can be modulated through the introduction of impurities, called dopants. Inorganic semiconductors are crystals such as GaN, with energy bands for electrons. The highest occupied energy band is called the valence band which is completely filled with electrons for an undoped semiconductor, while the next band higher in energy is called the conduction band and is empty. The energy difference between the minimum of the conduction band and the maximum of the valence band is called the bandgap of the semiconductor [1]. When there is an electron in the conduction band and an empty state or hole in the valence band the electron may combine with the hole and release the energy difference. This released energy can be in the form of a photon producing light.

LEDs are built in layers, a p-type semiconductor, an n-type semiconductor, and a depletion zone in between, creating the p-n junction that comprises the LED. The p-type and n-type semiconductors are created by doping existing semiconductors to either take away or add electrons, allowing one side to carry a negative charge (n-type) and the other to carry a positive charge (p-type). These semiconductors are combined so that under an electrical bias, electrons

and holes flowing in opposite directions meet in the p–n junction and recombine to emit photons [1].

Although silicon has been the favorite material for LEDs, in recent years GaN is turning out to be more promising material. GaN has a bandgap (E_g) of 3.4 electron volts (eV), while silicon's bandgap is only 1.1 eV. Since GaN has a bandgap that is nearly triple that of silicon, one needs significantly more energy to excite a valence electron into the conduction band of GaN. This limits GaN's usage in very low voltage applications (voltage required $V=E_g/e$), but on the other hand it allows GaN to stand larger breakdown voltages and have better thermal stability at higher temperatures[2]. Silicon is also an indirect band-gap semiconductor meaning the recombination process between an electron and a hole is not direct, making it extremely inefficient [3]. Furthermore, silicon has an electron mobility of 1500 cm^2/Vs, while gallium nitride has an electron mobility of 2000 cm^2/Vs. Therefore, the electrons in GaN crystals can move over ~ 30% faster than in Si crystals. This electron mobility gives GaN a distinct advantage as it can handle higher switching frequencies than silicon [2].

GaN nanowires in nanowire-LEDs are p-n junctions with the p-GaN on top and the n-GaN on the bottom. In between, there are 10 layers of InGaN composing the multiple quantum wells (MQWs) in the depletion zone. The InGaN allows its bandgap to be tuned by varying the amount of indium in the alloy. $In_xGa_{1-x}N$ has a direct bandgap which spans from the infrared (0.69 eV) for InN to the ultraviolet (3.4 eV) for GaN [4, 5]. This allows GaN made devices to cover the entire visible light spectrum. In general the GaN nanowire is 10-40 nm in diameter while the maximum length is about 500 μm. In spite of the positive properties of GaN-based nanowire LEDs discussed above there is a major problem. These devices with ITO (or conventional) electrodes have been known to suffer from poor Ohmic contact and injection current distribution. Contact refers to the metal-semiconductor (MS) junction which is responsible for current injection from the metallic lead to the semiconducting device. An Ohmic contact is a junction between two conductors that has a linear current-voltage (I-V) curve as with Ohm's law. In LEDs Ohmic contact is preferred as non-Ohmic contact has higher contact resistance (leading to large energy loss) which can result in less light production overall. Graphene electrodes show a better Ohmic contact characteristic than the ITO or conventional electrodes.

Graphene is an allotrope of carbon in the form of a single layer of atoms in a two-dimensional hexagonal lattice in which one atom forms each vertex. It can also be considered as an indefinitely large aromatic molecule. Graphene has many unique properties, most notably is its high thermal and electrical conductivities and optical transparency. In this research, we mainly focus on Graphene's low resistivity as a means to decrease the overall operating temperature of a nanowire LED [6].

In this paper, I present the schematic drawing of the device and the nanowire. Additionally, I present the experimental data measuring the voltage and current across the ITO and graphene devices. The steeper graphene curve indicates that it has a smaller resistance.

This means less input energy is wasted during the current injection, therefore, more input energy contributes to the electron-photon conversion processes resulting in graphene having a higher efficiency. A high contact resistance can also lead to high junction temperature, as the input energy can either be converted to light (photon) or heat. A high junction temperature leads to decrease of the efficiency as it makes value A and C increase. (see below for the definition of A and C values)

Next, using the experimental measurements of the IQE values as a function of the current density for thin film LED, ITO electrode LED and graphene electrode LED, I fit the parameters of the ABC model (see below) of each device. The fitted curves using this model give the values of the three parameters A, B, and C for each device (see Table). Finally I analyze and compare the A, B, and C values of the three separate devices to provide evidence that the graphene layer increases the overall performance of the device.

2. THEORETICAL MODELING

To ascertain the efficiency of any photosensitive device such as an LED one must look at the internal quantum efficiency (IQE). IQE relates the number of photons generated in the active region and the number of electrons injected into the LED. The IQE measures the ratio of electron-hole recombination that results in a photon to the total amount of recombination [7]. The IQE of the device can be described by the equation,

$$IQE = \frac{B N^2}{AN + B N^2 + C N^3},$$

where N represents the carrier density of the LEDs, A and C are the Shockley-Read-Hall (SRH) and Auger recombination rates respectively, and B represents the radiative recombination rate [8, 9]. Recombination of electrons and holes is a process by which electrons and holes annihilate each other: electrons fill up - through one or multiple steps - the empty state associated with a hole [10]. Both electrons and holes eventually disappear in this process. The energy difference between the initial and final state of the electron is released. In the case of radiative recombination, this energy is released as a photon. In other recombination processes the energy is essentially lost as heat. As temperature increases the values of A and C increase whereas the value of B decreases, causing a drop in the IQE. This leads to the deterioration of the performance of the LED device with increasing temperature.

3. METHODS AND MATERIALS

Different nanowire LED samples were fabricated. Fig. 1 is a model of the device. The device is built upon a substrate made out of sapphire and where GaN nanowires are placed on GaN. On top of the layer of nanowires is a graphene layer that allows light to pass through.

On top of the graphene layer is the p-type semiconductor while on the GaN layer is the n-type semiconductor. Fig. 2 shows the measured I-V curves at room temperature and Fig. 3 gives IQE (same as EQE in the figure) vs the carrier density. It can be seen that samples with graphene electrodes appear to have a lower contact resistance than the one with conventional ITO and films. Figure 3 shows the fit of the ABC model to the measured IQE values for the graphene, ITO and thin film devices. A comparison of the theoretical ABC model with experimental data shows that there is a good fit, particularly at high current densities. The values of parameters A, B, C obtained by fitting the experimental data are given in Table 1. The fabrication process of this device will be published in a separate paper.

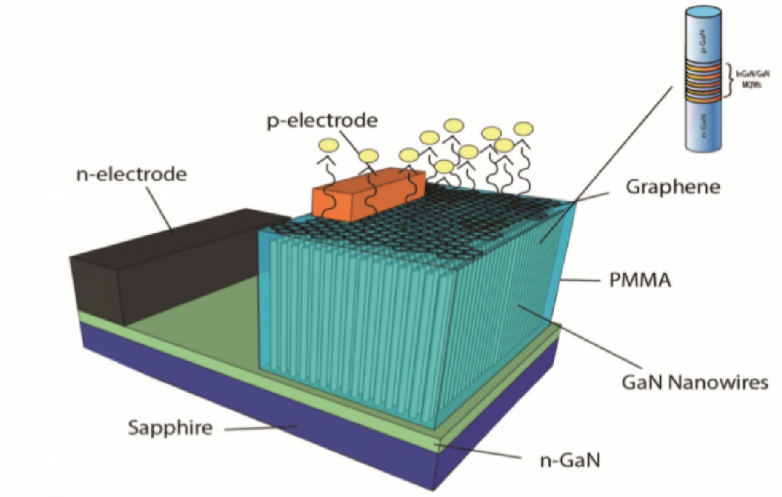

Figure 1: The schematic of a nanorod LED with graphene electrode as a current spreading electrode. Also shown is the illustration of the designs of a single nanorod LED.

Table

Sample	A	B	C
Thin Film	5.71E8	2.00E-11	6.91E-29
ITO	1.15E8	9.81E-10	6.51E-29
Graphene	7.91E7	9.95E-10	1.335E-29

4. RESULTS AND DISCUSSION

By comparing the A, B, and C values for the three types of devices we observe an increase in the B values and a decrease in the A and C values as we go from thin film to graphene. This is due to the increase in the radiative recombination process caused by less structural defects and a decrease in the polarization-induced electric field of the device. The polarization-induced electric field is known to cause efficiency drops due to its increase of the electron leakage in MQWs. The decreasing of this polarization caused by less strain from the nanowires therefore leads to more radiative recombination.[11] The decrease in the A and C values implies a decrease in the trap-recombination and auger recombination respectively.

Although our measurements are done at 300 K we can make some qualitative remarks on the effect of temperature on the relative importance of the three recombination rates. In an intrinsic semiconductor when temperature is increased the number of thermally excited electrons in the conduction band and holes in the valence band increases. [12]. As carrier concentration increases the cubic dependence (the C term) associated with the Auger process becomes more prominent causing a large efficiency drop. The ratio of BN^2/CN^3 will reduce to B/CN thus decreasing the IQE as there is less radiative recombination per total recombination. As observed, the curves representing the thin films, nanowires, and graphene the drop becomes less evident as you progress to the latter. This demonstrates that graphene has the highest IQE overall along with the lowest efficiency drop due to its high B value and small A, C values. These results can also be viewed in the graph comparing thin film, ITO and graphene (Figure 3) where graphene has the highest curve with the smallest drop.

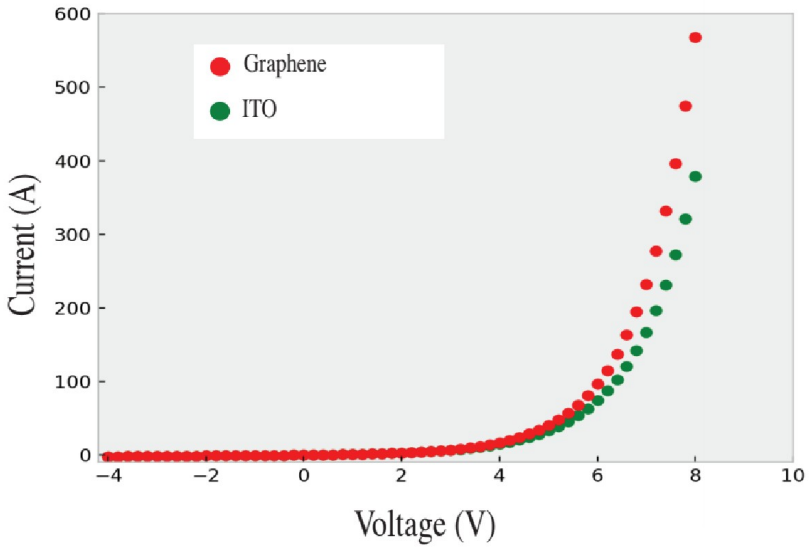

Figure 2: Measured Room temperature I-V characteristics of GaN nanorod LEDs with ITO and grapheme

A change in temperature also affects the voltage at the diode. As the temperature increases, the carrier concentration increases. The increase in energy from the increase in temperature allows more electrons to cross the band gap, going from the valence band to the conduction band and leaving behind a hole. The intrinsic carrier concentration being the number of electrons in the conduction band, thus increases.

We next discuss qualitatively the reason behind the change in voltage. The fermi level is defined as the probability for occupancy of an electron above or below the energy level. The probability of finding an electron above the fermi level is the same as the probability of not finding an electron below. In an n-type semiconductor the number of electrons in the conduction band is greater than the number of holes in the valence band, due to doping. This results in a fermi level that is closer to the conduction band. With the increase in intrinsic carrier concentration due to the increase in temperature, in the n-type semiconductor the intrinsic carriers will dominate the donors. To maintain the balance of the carrier density on both sides the fermi level in the n-type will gradually shift downwards, towards the intrinsic fermi level in the middle of the bandgap. Similarly in the p-type as temperature increases the fermi level will shift from the valence band towards the middle of the band gap. Since the built-in potential of a diode is determined by the difference in fermi-levels in the p-type and n-type regions, as the fermi level in each region moves closer to the middle of the gap, the built-on potential is decreased. As this potential decreases the voltage across the device also decreases. As voltage and current are directly proportional, this will result in a decrease in current. This results in a decrease in the charge carriers in the active region, which results in less radiative recombination meaning a decrease in efficiency and light production overall [10].

Finally, the power P generated in a device of resistance R and current I is $P = I^2R$. This means a decrease in the current decreases the power output of the device. Overall, Graphene is shown to be an effective solution to decrease the operational temperatures of the devices. Due to its low resistivity graphene will generate less heat, leading to a slower increase in operational temperature in addition to having an operational temperature lower than that of the ITO. Graphene's greater current given an applied voltage, in comparison to the ITO can be observed in Figure 2. [13]

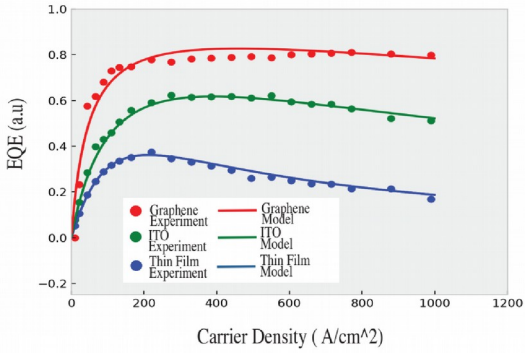

Figure 3: Measured EQE and simulated IQE for samples with different types of electrodes.

ACKNOWLEDGEMENT

Several people played a role in the accomplishment of this paper, and I would like to thank all of them. I am thankful to my Research Guide Dr. Shaofei Zhang (University of McGill) for his valuable guidance, encouragement, and knowledge during the course of this research and its presentation. I am also thankful to Supervisor Dr. Alex Zang (University of McGill) who went out of his way to provide me with help and support, and also accompany me to the conference, resulting in the successful project. I am also very grateful to Dr. Subhendra D Mahanti (Michigan State University) for giving me the opportunity to write this paper, and for his thoughtful and careful deliberation along the way.

REFERENCES

1. Neamen, Donald A. Semiconductor Physics and Devices: Basic Principles. McGraw-Hill, 2012.
2. "GaN vs. Silicon: Semiconductor Materials Compared." Arrow.com, 30 Jan. 2020, www.arrow.com/en/research-and-events/articles/gan-vs-silicon-semiconductor-materials-compared.
3. Gayral, Bruno. "LEDs for Lighting: Basic Physics and Prospects for Energy Savings." Comptes Rendus Physique, vol. 18, no. 7-8, 2017, pp. 453–461., doi:10.1016/j.crhy.2017.09.001.
4. Suo, Guoquan, et al. "Synthetic Strategies and Applications of GaN Nanowires." Advances in Condensed Matter Physics, vol. 2014, 2014, pp. 1–11., doi:10.1155/2014/456163.
5. Yang, G.f., et al. "InGaN/GaN Multiple Quantum Wells on Selectively Grown GaN Microfacets and the Applications for Phosphor-Free White Light-Emitting Diodes." Reviews in Physics, vol. 1, 2016, pp. 101–119., doi:10.1016/j.revip.2016.06.001.
6. Michael, and Berger. "What Is Graphene?" Nanowerk, Nanowerk, 11 Sept. 2019, www.nanowerk.com/what_is_graphene.php.
7. D.A.Laleyan, "Design, Epitaxial Growth and Characterization of Nanowire Light Emitting Diodes", 2014.
8. Dai, Qi, et al. "Carrier Recombination Mechanisms and Efficiency Droop in GaInN/GaN Light-Emitting Diodes." Applied Physics Letters, vol. 97, no. 13, 2010, p. 133507., doi:10.1063/1.3493654.
9. Nguyen, H. P. T., et al. "p-Type Modulation Doped InGaN/GaN Dot-in-a-Wire White-Light-Emitting Diodes Monolithically Grown on Si(111)." Nano Letters, vol. 11, no. 5, Nov. 2011, pp. 1919–1924., doi:10.1021/nl104536x.
10. V., Van Zeghbroeck Bart. Principles of Semiconductor Devices and Heterojunctions. Prentice Hall, 2010.
11.Ryu, H. Y., et al. "A Comparative Study of Efficiency Droop and Internal Electric Field for InGaN Blue Lighting-Emitting Diodes on Silicon and Sapphire Substrates." Scientific Reports, vol. 7, no. 1, 2017, doi:10.1038/srep44814.
12. Nguyen, Hieu Pham Trung, et al. "Controlling Electron Overflow in Phosphor-Free InGaN/GaN Nanowire White Light-Emitting Diodes." Nano Letters, vol. 12, no. 3, Feb. 2012, pp. 1317–1323., doi:10.1021/nl203860b.
13."Does Dimming LEDs Decrease Their Lamp Life?: LED Lighting Systems: Lighting Answers: NLPIP." *Does Dimming LEDs Decrease Their Lamp Life? | LED Lighting Systems | Lighting Answers | NLPIP*, www.lrc.rpi.edu/programs/nlpip/lightinganswers/led/dimmingLampLife.asp.

STUDENT JOURNAL OF PHYSICS

Volume 8 **Number 2** **2020**

CONTENTS

ARTICLES